The Sun at millimeter wavelengths

III. Impact of the spatial resolution on solar ALMA observations

Henrik Eklund[1,2], Sven Wedemeyer[1,2], Mikołaj Szydlarski[1,2], and Shahin Jafarzadeh[1,2]

[1] Rosseland Centre for Solar Physics, University of Oslo, Postboks 1029 Blindern, 0315 Oslo, Norway
e-mail: henrik.eklund@astro.uio.no
[2] Institute of Theoretical Astrophysics, University of Oslo, Postboks 1029 Blindern, 0315 Oslo, Norway

ABSTRACT

Context. Interferometric observations of the Sun with the Atacama Large Millimeter/sub-millimeter Array (ALMA) provide valuable diagnostic tools for studying the small-scale dynamics of the solar atmosphere.
Aims. The aims are to perform estimations of the observability of the small-scale dynamics as a function of spatial resolution for regions with different characteristic magnetic field topology facilitate a more robust analysis of ALMA observations of the Sun.
Methods. A three-dimensional model of the solar atmosphere from the radiation-magnetohydrodynamic code Bifrost was used to produce high-cadence observables at millimeter and submillimeter wavelengths. The synthetic observables for receiver bands 3–10 were degraded to the angular resolution corresponding to ALMA observations with different configurations of the interferometric array from the most compact, C1, to the more extended, C7. The observability of the small-scale dynamics was analyzed in each case. The analysis was thus also performed for receiver bands and resolutions that are not commissioned so far for solar observations as a means for predicting the potential of future capabilities.
Results. The minimum resolution required to study the typical small spatial scales in the solar chromosphere depends on the characteristic properties of the target region. Here, a range from quiet Sun to enhanced network loops is considered. Limited spatial resolution affects the observable signatures of dynamic small-scale brightening events in the form of reduced brightness temperature amplitudes, potentially leaving them undetectable, and even shifts in the times at which the peaks occur of up to tens of seconds. Conversion factors between the observable brightness amplitude and the original amplitude in the fully resolved simulation are provided that can be applied to observational data in principle, but are subject to wavelength-dependent uncertainties. Predictions of the typical appearance at the different combinations of receiver band, array configuration, and properties of the target region are conducted.
Conclusions. The simulation results demonstrate the high scientific potential that ALMA already has with the currently offered capabilities for solar observations. For the study of small-scale dynamic events, however, the spatial resolution is still crucial, and wide array configurations are preferable. In any case, it is essential to take the effects due to limited spatial resolution into account in the analysis of observational data. Finally, the further development of observing capabilities including wider array configurations and advanced imaging procedures yields a high potential for future ALMA observations of the Sun.

Key words. Sun: chromosphere – Sun: radio radiation – Sun: atmosphere – shock waves – techniques: interferometric – Sun: oscillations

1. Introduction

The Atacama Large Millimeter/sub-millimeter Array (ALMA) provides great advances in observing the small-scale dynamics of the solar atmosphere for the more direct measurement of chromospheric temperatures as compared to other diagnostics. The millimeter (mm) and submillimeter (submm) wavelength radiation that is observable with ALMA originates from the free-free emission at chromospheric heights and is formed in local thermal equilibrium (LTE; see, e.g., Wedemeyer et al. 2016, and references therein). The measured intensities, which are usually expressed equivalently as brightness temperatures (T_b), therefore have a linear relation to the local plasma temperature over the mapped atmospheric height range.

Now, several years since the first solar ALMA observations, a number of studies of ALMA data have been reported. Some of them address the small-scale dynamics, for example, that of magnetic field loop structures (Wedemeyer et al.

2020), on-disk type II spicules (Chintzoglou et al. 2021a), spicules at the limb (Shimojo et al. 2020), and transient brightening events with corresponding brightness temperature evolution (Shimojo et al. 2017; Molnar et al. 2019; da Silva Santos et al. 2020; Nindos et al. 2020; Eklund et al. 2020; Chintzoglou et al. 2021b), spectral sub-bands (SB) are used to estimate the optical thickness (Rodger et al. 2019), and the dynamical structure in and around sunspots (Jafarzadeh et al. 2019) and of the oscillations in ALMA observations (Patsourakos et al. 2020; Guevara Gómez et al. 2021; Jafarzadeh et al. 2021) is studied. Eklund et al. (2020) systematically detected small-scale dynamics and brightening events in ALMA band 3 observations. The statistical analysis of the detected events revealed that the magnitude of the excess in brightness temperature is smaller than what is predicted based on one-dimensional (1D) simulations (Loukitcheva et al. 2004, 2006). The spatial sizes of the detected events show a distribution that increases in number toward the lower angular resolution limit ($1\overset{''}{.}4 - 2\overset{''}{.}1$), suggesting that there may be

many more events at smaller scales that are unresolved so far. The spatial resolution of currently possible ALMA observations of the Sun ranges from approximately 0″.7 and upward to several arcsec, for instance, 4″.5 or 8″.1 (Nindos et al. 2018, 2020), depending on the receiver band and array configuration. Chromospheric small-scale dynamic structures, with a variety of spatial and temporal scales, have also been studied with diagnostics at shorter wavelengths (e.g., optical), allowing for a higher spatial resolution, which again depends on the size of the telescopes that are employed (see, e.g., van Noort & Rouppe van der Voort 2006; Wöger et al. 2006; Rouppe van der Voort et al. 2009; Borrero et al. 2017; Gafeira et al. 2017). These have resulted in observations of small-scale structures that currently cannot be resolved with ALMA. As a consequence, the magnitude of the corresponding brightness temperature (T_b) variations of the small-scale dynamics is significantly affected. Studies of radiative mm wavelength maps from simulations show that the T_b excess due to dynamic shock wave signatures is reduced due to limited spatial resolution (Wedemeyer-Böhm et al. 2007).

Eklund et al. (2021) characterized the observable brightening signature from propagating shock waves in the synthetic observables at mm wavelengths from the numerical 3D magnetohydrodynamical Bifrost (Gudiksen et al. 2011; Carlsson et al. 2016) model, and Eklund et al. (2020) showed that degrading the resulting brightness temperature maps to the resolution of the observations reduces the resulting magnitude of the T_b excess of the brightening events. This in turn leads to a better agreement with the observational findings. The degree of degradation of the small-scale dynamic signatures is clearly dependent on the spatial resolution, but also on the distribution of the spatial scale and on the contrasts of the target. The spatial resolution of an interferometer such as ALMA is mainly dependent on the physical positions of the antennas and the wavelength of the observations. The spatial resolution also crucially affects the identification of oscillatory signals in the solar atmosphere (Jess et al. 2021a,b). In particular, a higher quiet-Sun energy flux (at a similar atmospheric height and frequency range) was found by Bello González et al. (2010) from observations with a 1 m solar telescope as compared to observations with a 0.7 m telescope by Bello González et al. (2009). We use a state-of-the-art Bifrost simulation (Gudiksen et al. 2011; Carlsson et al. 2016) here to perform estimations of how the observable small-scale dynamic signatures at mm and submm wavelengths in both the spatial and temporal domain are affected by the degradation of the spatial resolution corresponding to ALMA observations.

This paper is the third in a paper series. The first paper by Wedemeyer et al. (2020) presented an analysis of one of the first regular band 3 observational data sets of the Sun and evaluated the limitations and quality of the data. The second paper in the series (Eklund et al. 2020) used the same observational data set to detect and study the evolution of dynamic small-scale brightening events. It concluded that the angular resolution is crucial to interpret the data. This third paper in the series is structured as follows. In Sect. 2 we present the numerical simulation that is used in the study and detail the calculation of the mm wavelength observables and degradation process to the spatial resolutions corresponding to ALMA observations. In Sect. 3 we present the resulting observables of the respective ALMA spectral bands. We also show the effects of limited spatial resolution on dynamical small-scale signatures in the spatial and temporal domains. Finally, in Sect. 4 we discuss some clarifications and comparisons with observational data, which are followed by conclusions in Sect. 5.

2. Methods

2.1. 3D magnetohydrodynamic simulations

A solar atmospheric numerical 3D model from the radiation-magnetohydrodynamic code Bifrost (Gudiksen et al. 2011; Carlsson et al. 2016) was used, where nonlocal thermodynamic equilibrium (non-LTE) and hydrogen ionization in non-equilibrium were considered. The simulation box extends 24 Mm in horizontal directions (x, y) and 17 Mm in vertical direction (z). In each horizontal direction there are 504 cells with a uniform grid spacing of 48 km (corresponding to an angular size of approximately 0.066 arcsec), while in the vertical direction were 496 cells with a grid spacing between 19 and 100 km. At chromospheric heights, most relevant to this work, the vertical grid spacing is 20 km. The horizontal directions has periodic boundary conditions. The bottom boundary was located at a depth of 2.5 Mm below the solar photosphere. The total duration of the simulation sequence considered here was approximately one hour with an output cadence of 1 s to match the (currently) highest cadence of ALMA observations in solar mode. The first 200 s of the simulation were excluded from the analysis to ensure that a quasi-equilibrium state was reached. The simulation represents quiet-Sun conditions, but also includes a magnetic field region of opposite polarity in the center, in which the polarity patches are approximately 8 Mm apart (Carlsson et al. 2016). At photospheric heights, the overall unsigned magnetic field strength has a value of 50 G. The same model was used in Wedemeyer et al. (2020) to study the diagnostic potential of ALMA observations of the Sun and in Eklund et al. (2021) to determine the underlying physical conditions and mm wavelength signatures due to propagating shock waves. The same model setup, but with a lower cadence, was also used in Loukitcheva et al. (2015, 2017) to analyze chromospheric diagnostics at mm and submm wavelengths. The magnetic topology of the simulation from the photosphere to the chromosphere and transition region is illustrated in Fig. 1 of Jafarzadeh et al. (2017), where the authors show that the height of magnetic canopies (i.e., when the field lines bend over from nearly vertical at low altitudes to more horizontal configurations at higher altitudes; Solanki & Steiner 1990; Wedemeyer-Böhm et al. 2009) throughout the solar atmosphere depends on the strength of the magnetic fields at their footpoints in the low photosphere.

2.2. Brightness temperature maps at mm wavelengths corresponding to ALMA observations

The intensities at mm wavelenghts are obtained by solving the radiative transfer equation column-wise throughout the FOV, using the advanced radiative transfer (ART) code (de la Cruz Rodríguez et al. 2021)[1]. LTE conditions in the formation of the radiation are assumed, but relevant sources of opacity are included in detail by the code.

The intensities were calculated at frequencies corresponding to the (spectral) receiver bands of ALMA, with ten frequencies equidistantly distributed across the spectral range of each receiver band. The spectral setup of the receiver bands is presented in Table 1 (see Table A.1 for the specific frequencies that were used in the calculations for each receiver band). Average values of the intensities at all the ten frequencies were used in the analysis because they are a good approximation for the continuum maps derived from actual observations. Receiver bands
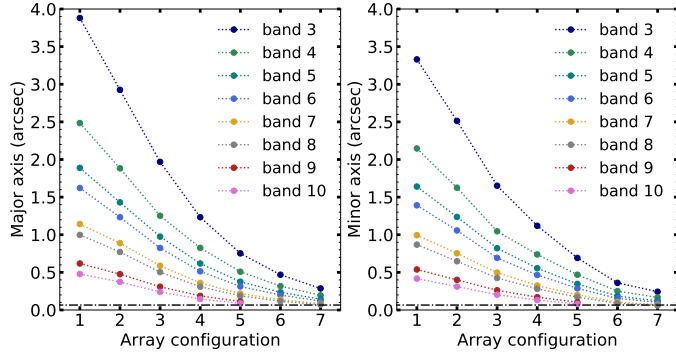
---

[1] https://doi.org/10.5281/zenodo.4604825

Fig. 1. Major and minor axes of the clean beams corresponding to the respective combination of spectral band and array configurations C1–C7. The values represent the FWHM along the axes of the clean beams for the full spectral width of the receiver bands at a fixed time. The horizontal dot-dashed black lines mark the limit of the cell size of 0.066 arcsec of the original model.

Table 1. Wavelengths and frequencies of the ALMA receiver bands assumed here.

Receiver band	Wavelength [mm] min	max	Frequency [GHz] min	max
3	2.7759	3.2586	92.0	108.0
4[(†)]	1.9594	2.1883	137.0	153.0
5	1.4553	1.5779	190.0	206.0
6	1.2040	1.3091	229.0	249.0
7	0.8454	0.8854	338.6	354.6
8[(†)]	0.7259	0.7551	397.0	413.0
9[(†)]	0.4441	0.4495	667.0	675.0
10[(†)]	0.3442	0.3474	863.0	871.0

Notes. Receiver bands 4, 8, 9, and 10 (marked with a dagger [(†)]) are not yet commissioned for solar observations and were assumed to be symmetrically distributed around the "standard continuum" central frequencies (see, e.g., Table 6.1 in the ALMA technical handbook Remijan et al. 2020), similar to those of the commissioned bands.

3, 5, 6, and 7 are currently offered for solar ALMA observations. The specified wavelengths we used here are from observational cycle 8. For the remaining spectral bands (4, 8, 9, and 10), the central frequencies were taken to be those of the standard continuum exemplary values (Table 6.1 in the technical handbook for ALMA cycle 8[2]; Remijan et al. 2020). The spectral setup of these bands is symmetric around the corresponding central frequencies with a separation of 5 GHz in bands 4 and 8 and 2 GHz in bands 9 and 10 (see Table A.1). If the remaining receiver bands were considered for solar observations, the resulting exact frequencies might differ slightly from what we used here, but the results still serve as a good estimate for what to expect from such potential observations.

At the mm and submm wavelengths of the ALMA receiver bands, the Rayleigh-Jeans approximation holds and the radiative intensities (I_λ) can be translated into brightness temperatures (T_b) through the relation

$$T_b = \frac{\lambda^4}{2 k_B c} I_\lambda, \tag{1}$$

where λ is the wavelength, k_B is the Boltzmann constant, and c is the speed of light of the radiation.

2.3. Spatial resolution of ALMA observations

The spatial resolution of the interferometric array is determined by the lengths of the baselines, which are the distances between each pair of antennas. The array can be reconfigured by physically moving some of the 12 m antennas, which thus changes the distribution of covered baselines. This is done in stages throughout the observational cycles, from the most compact array configuration C1 with a maximum baseline length of 0.16 km to array configuration C10, which has a maximum baseline length of 16.2 km.

For a highly dynamic target such as the Sun, a high temporal cadence is required to capture the small-scale dynamic structures, which for long baselines comes with complications in the reconstruction of the data due to atmospheric disturbances. So far (as of observational cycle 8), only the most compact array configurations, C1 to C4 at band 3, C1 to C3 at band 5 and

band 6, and C1 to C2 at band 7, are offered for solar observations. In this study, we also report estimations corresponding to a few more extended array configurations as a means of predicting the future potential for solar observations. We limit the study to array configuration C7, with a maximum baseline of 3.6 km because configurations that are even more extended, if feasible at all for solar observations, would require substantial development and commissioning efforts and are therefore not likely to be realized in the near future.

The shape of the point spread function (PSF) of an interferometric observation is mostly the result of the specific combination of frequencies, array configuration, and the target position on the sky relative to the baselines of the array. The sidelobes of the PSF are usually removed through a deconvolution technique, such as the commonly used CLEAN algorithm (Högbom 1974). The remaining main-lobe of the PSF, also referred to as the 'clean beam', represents the effective resolution element of the observation. This work shows the possibilities of observing small-scale dynamics from an optimistic perspective of a best-case scenario that corresponds to a perfectly sampled observation. Uncertainties coming from, the undersampled Fourier space, noise, and data reconstruction artifacts, for instance, would need to be added, but they are beyond the scope of the first step presented here (more about this in Sect. 4.2). Synthetic ALMA observations with specific frequencies and bandwidths of the receiver bands and sub-bands (cf. Table 1) and with different array configurations were constructed using the simobserve[3] task included in the Common Astronomy Software Applications (CASA)[4] package. The clean beams were then extracted from the resulting measurement sets of the synthetic observations and were used as kernels in 2D convolution of the respective brightness temperature maps.

The shape of the clean beam is determined by the projected baselines on the plane of the sky perpendicular to the target source (or in other words, how the interferometric array would be seen from the target). The shape of the clean beam therefore varies with the time of the day and becomes more eccentric with increasing angular distance between the target and zenith.

---

[2] https://almascience.eso.org/documents-and-tools/cycle8/alma-technical-handbook

[3] Info about the simobserve tool can be found here: https://casa.nrao.edu/casadocs-devel/stable/global-task-list/task_simobserve/about.

[4] https://casa.nrao.edu

The location of the Sun on the sky is therefore very important to consider when studying small-scale features. As a first approximation, we placed the Sun at an angle close to zenith, which resulted in a slightly eccentric clean beam. This choice is representative of many solar data sets found in the ALMA Science Archive[5] to this date. The minor and major axes of the clean beams for each spectral band and array configuration are given in Fig. 1 (numerical values are listed in Table A.2).

3. Results

3.1. Brightness temperature maps

The brightness temperature (T_b) maps resulting from the radiative transfer calculations on the Bifrost model as seen from the model top (corresponding to a solar disk-center position) are presented in Fig. 2 for bands 3 and 6. The T_b maps are given at the original resolution of the model and at the degraded resolutions corresponding to those of array configuration C3 for the respective band. These bands and resolutions were chosen specifically as illustrative examples, as they represent the so-far most commonly used combinations of receiver bands and configurations for solar observations. The other combinations of receiver bands and resolutions are illustrated in Fig. A.2 for reference. The brightness temperatures represent the full-band averages (see Table 1). The typical contrasts and scales vary with frequency as a result of the varying formation height in the solar atmosphere (see Sect. 3.2 for more information). The analysis is focused on three regions with different typical characteristics, which are marked in Fig. 2. One inter-network quiet-Sun region (QS) and two enhanced network regions, one located straight above one of the footpoints of the magnetic loop structures (FP) and one in between the footpoints, where filamentary structures (FS) can be seen in the magnetic field loops.

3.2. Formation heights

The mm and submm wavelength radiation is highly sensitive to the dynamics of the chromosphere (Loukitcheva et al. 2004, 2006), and the formation heights varies strongly with time. The radiation at a given wavelength originates in an extended range of heights with one or more main contributing component(s). The height of optical depth $\tau = 1.0$ (at the considered observing wavelength λ) often serves as a good approximation for the most dominant component. The formation heights of optical depth unity ($z(\tau_\lambda = 1.0)$) are presented in Fig. 3 for the entire FOV of bands 3 and 6 at one time step ($t = 1650$ s), together with histograms of the distributions for the time range $t = 1000–2000$ s for all receiver bands. The mean values of the formation height distribution at each band are marked at the x-axis of each corresponding region in Fig. 3. The mean formation height of the radiation increases with wavelength.

The structures above ~1.5 Mm are more extended horizontally in band 3 than in band 6 (see Fig. 3), which suggests that these structures expand with height. This is also reflected in the formation height distribution in Fig. 3, where band 3 shows significant enhancement at large heights in all the three regions compared to the other bands. This effect is most notable at heights around 1.3–1.8 Mm in the QS region and around 2.2–2.5 Mm in the FS region. Most of the receiver bands show multiple components in the formation height distributions, and the height of the peaks differs between the regions. For instance,

in the QS region, the FOV is dominated by propagating shock waves and intermediate post-shock regions. The radiation at mm wavelengths efficiently tracks a shock front as it propagates upward through the mid-chromosphere (Eklund et al. 2021). At a certain height that depends on the observed wavelength, the radiation starts to decouple from the shock front and instead originates in lower heights in the now visible post-shock region. The coupling of radiation at mm wavelengths to the rapidly propagating shock fronts results in a poorer representation of the formation heights in the mid-chromosphere (cf. Fig. 3 in Eklund et al. 2021). This under-representation can be seen in the QS formation height distributions in Fig. 3, in particular, for heights of about 1.35 Mm in band 3, 1.1 Mm in band 6, and 1.0 Mm in band 7. Bands 9 and 10 do not show a double-component distribution for the QS region, which suggests that they do not map the upward-propagating shock fronts. These bands instead map heights in which propagating waves have not yet fully developed into shocks. This agrees with the typical heights seen for the onset of shock formation in the 3D numerical model (see also, e.g., Wedemeyer et al. 2004).

In the enhanced network regions, FS and FP, bands 9 and 10 mostly map the lower layers around 0.5–0.8 Mm, whereas the lower receiver bands show larger formation heights than in the QS region. With decreasing receiver band number, the magnetic loops are more efficiently mapped. The loops are present in a range of heights and give rise to corresponding peaks in the formation height distributions around 1.9 Mm and 2.4 Mm for band 3 and around 1.5 Mm for band 6 (see Fig. 3). The height range below the magnetic loops (hereafter also referred to as subcanopy domain) is also partly sampled in band 6, which is reflected by the peak around 0.7 Mm in the formation height distribution plot.

At the longest wavelengths (i.e., band 3), the formation heights in the FS region are typically larger than 1.3 Mm, with a large peak at 1.9 Mm and another at around 2.4 Mm, indicating that band 3 maps the magnetic field loop structures at high altitudes (cf. Fig. 2). However, at shorter wavelengths (i.e., band 5 and below), an enhanced occurrence of formation heights around 0.7 Mm is seen in the FS region, which becomes more apparent at the even shorter wavelengths of bands 6–10. This suggests that with receiver bands 5–10, we partly see through the magnetic loops, but at band 3 (similarly at band 4), the magnetic loops are to a larger extent optically thick and do not allow mapping the layers at lower heights. The radiation in bands 9 and 10 in the FS region mostly originates at heights below the magnetic loops. This subcanopy contribution is also picked up by lower bands, although it decreases with receiver band number and is barely present for band 3. The magnetic loops are substantially opaque in band 3 but remain partly transparent in bands 5–7 and to a large extent completely transparent in bands 9–10. In addition, the loops are not distributed equally, so that the resulting formation height depends on the combination of the loop geometry at that location and on the opacity, which depends on the wavelength range mapped by the receiver bands. As a result, in some locations, an opaque magnetic loop lies in the line of sight, while it is possible to see farther down into the subcanopy domain at other locations. While the specifics depend on the receiver band, there is consequently a lack of radiation with formation heights at about 1.0 Mm for all bands.

3.3. Brightness temperature distributions

In Fig. 4 we show the brightness temperature distributions for the receiver bands 3−10 for the three selected regions, QS, FS, and
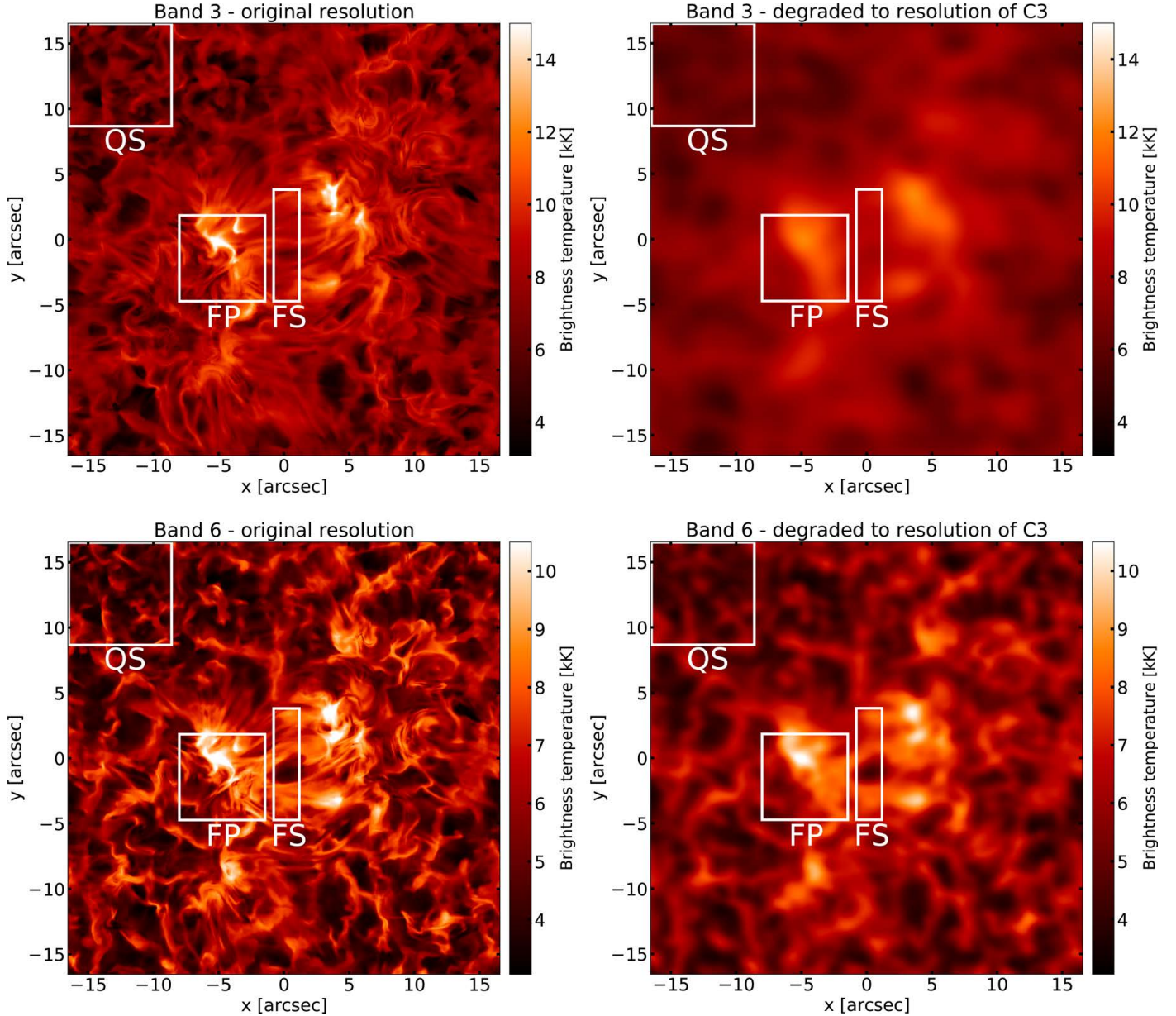
---

[5] https://almascience.nrao.edu/asax/

Fig. 2. Brightness temperature maps at selected frequencies within receiver band 3 (*upper row*) and band 6 (*lower row*) at original resolution (*left column*) and at degraded resolutions corresponding to observations with array configuration C3 (*right column*). Three selected regions are marked in the FOV: QS represents the quiet Sun, FP contains the footpoints of the prominent magnetic loops, and FS shows the loop structure between the two footpoints. The snapshots are taken at $t = 1650$ s. The brightness temperatures at original resolution span a range of 3.1 kK to 16.6 kK for band 3 and 2.9 kK to 11.3 kK for band 6, but are capped in the figure at 15 kK and 11 kK, respectively, to better illustrate less bright structures.

FP (cf. Fig. 2) for the time range $t = 1000$–2000 s. There are significant differences in the T_b distributions between the receiver bands, which is a direct result of sampling layers at different heights at the different wavelengths (see Sect. 3.2). In general, the mean value of the T_b distributions increases with wavelength for each of the three regions. This is expected for a monotonic increase in the average temperature in the chromosphere (see, e.g., Vernazza et al. 1981). However, there are large spans of brightness temperatures for each band and region. The T_b distributions are closely related to the formation heights because the observable intensity at a given wavelength, or here equivalently, the brightness temperature, is the result of the integrated contribution function over height z (Eklund et al. 2021),

$$T_b = \int_{-\infty}^{\infty} dz\, \chi_\nu T_g(z) e^{-\tau_\nu(z)}, \qquad (2)$$

where χ_ν is the opacity, T_g is the gas temperature, and τ_ν is the height dependent optical depth. This connection becomes very clear for the QS region (compare the top right panel in Fig. 3 with the top left panel in Fig. 4). The QS region shows the lowest mean temperatures, the FP region shows the highest temperatures, and the values for the FS region lie in between. The increase in T_b with magnetic activity is in line with recent band 3 ALMA observations (Wedemeyer et al. 2020). The shorter the wavelength (the higher the receiver band number), the smaller the change in mean temperature between the different regions. The visibility of the elongated structures connected to the magnetic loops in the FS region becomes poorer with increasing frequency as a result of the loop geometry in combination with the mapped formation height ranges. The magnetic field lines in the loops are largely vertical at low heights at the magnetic
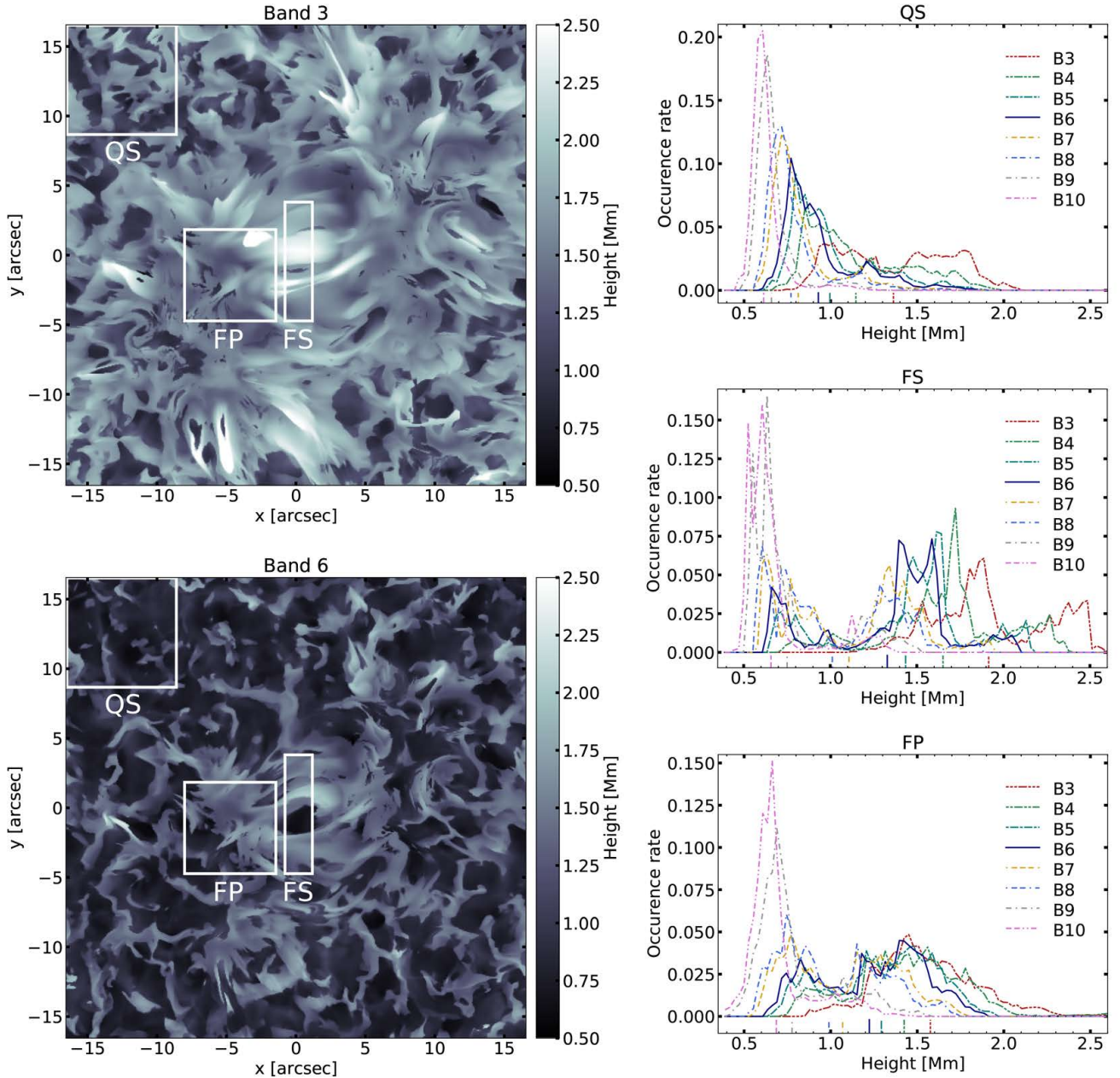
Fig. 3. Formation heights of the simulated continuum radiation at original resolution. *Left column*: formation heights for band 3 (*upper panel*) and band 6 (*lower panel*) at $z(\tau_\lambda = 1)$ for the entire FOV at $t = 1650$ s. The ranges of the FOV maps are given in the same color-scale to facilitate comparison, but the ranges span between 0.6–3.3 Mm and 0.5–2.3 Mm at band 3 and band 6, respectively. *Right column*: histograms of the formation heights $z(\tau_\lambda = 1)$ of all receiver bands (3–10) in the three defined areas, QS (*upper panel*), FS (*middle panel*), and FP (*lower panel*). The distributions are calculated for the time range of $t = 1000$–2000 s. The mean values of each distribution are indicated at the x-axes with matching line styles. The distributions are given with the same x-axis for convenience, but band 3 in the FP region in particular shows a small enhancement of up to 3 Mm.

footpoint (in the FP region), and they gradually bend with increasing height to become practically horizontal at some height.

The low brightness temperatures in the middle of the FS region in the band 6 map (see Fig. 2) are connected to low formation heights (see Fig. 3), implying that the subcanopy domain, (i.e., the volume under the largely horizontal overlying magnetic field lines; see Sect. 2.1) is visible at these locations. At smaller and larger y-coordinates, however, band 6 maps higher brightness temperatures at larger heights in the magnetic loops. Except for a very small patch, the subcanopy domain is not visible in band 3, in contrast, because essentially the whole region

is covered by magnetic loops that become opaque at heights above the subcanopy domain. Consequently, the FS region in the band 3 map is mostly filled with hotter filamentary structures. These wavelength-dependent trends can also be seen for the remaining receiver bands, which are given in Figs. A.1–A.2 for reference.

This thus suggests that it might be possible for these magnetic field loops to study the underlying structures with short wavelengths (specifically bands 9–10) and to effectively study the top of the loop structures at longer wavelengths (bands 3 and 4). Bands 7 and 8 map lower heights than bands 5 and 6 and might therefore be more suitable for studying upwardly
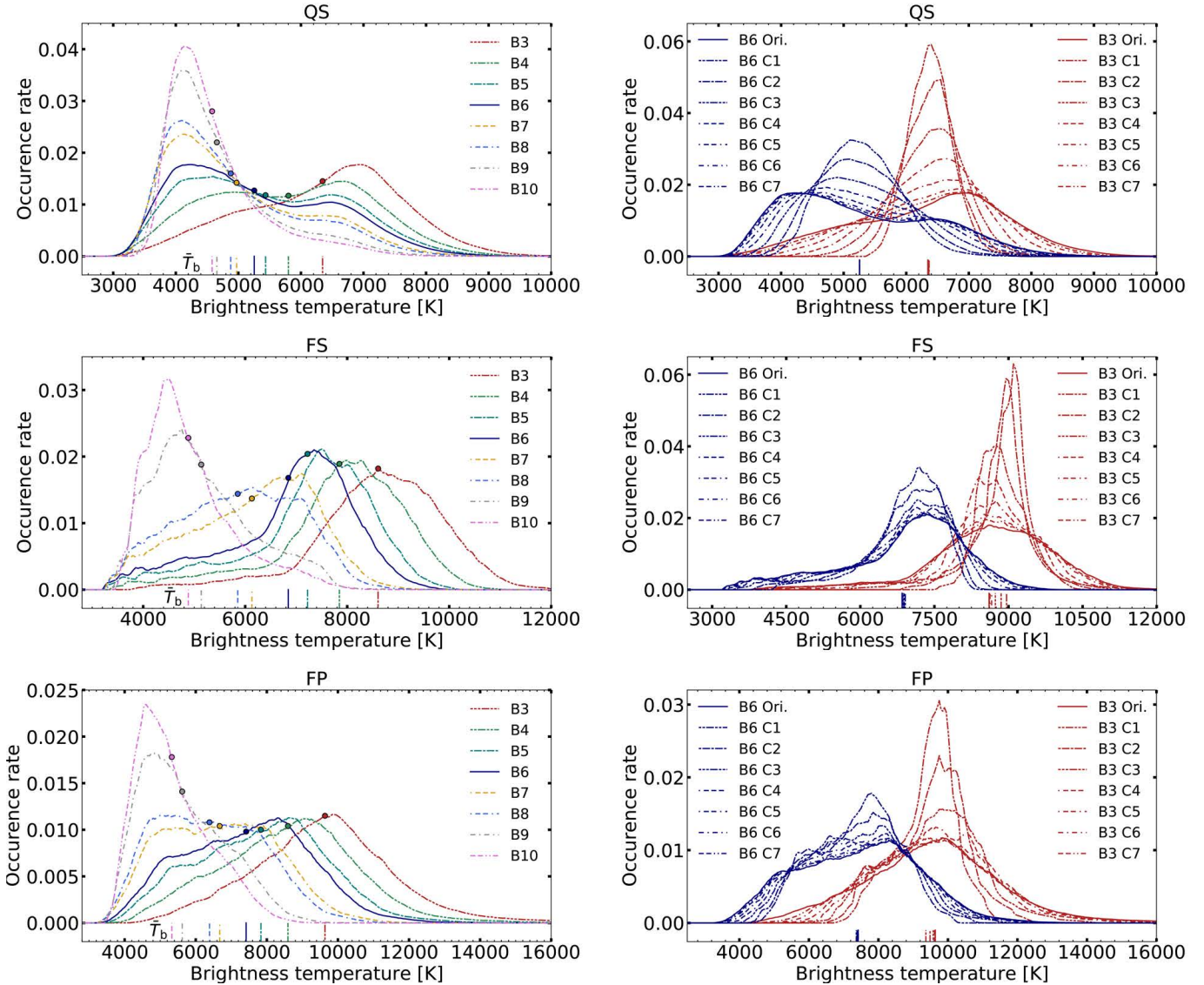
Fig. 4. Brightness temperature distributions corresponding to different receiver bands and array configurations. *Left column*: brightness temperature distributions at the original resolution for the respective spectral band in each of the three different regions. *Top left panel*: QS. *Middle left panel*: FS. *Bottom left panel*: FP. The circles mark the mean values of each distribution, whose values are also indicated at the *x*-axes. *Right column*: brightness temperature distributions of bands 3 and 6 at the resolutions of the original model and array configurations C1 to C7. The average values of each respective distribution are marked at the *x*-axes. The T_b scales are different in each row.

propagating waves etc., as they enter the height range in which magnetic loops potentially interfere with the waves. The effect of increasing formation height with wavelength and the dependence on the magnetic filling factor of the different regions is indicated in Fig. 4: mean temperatures between the different regions are similar in band 10 (4.58 kK, 4.48 kK, and 4.32 kK in QS, FS, and FP, respectively) but show a large increase in band 3 from QS (6.35 kK) to the network region FP (9.65 kK).

There are a cool component and a hot component in the T_b distributions (Fig. 4), although they are more or less apparent for the individual receiver bands. The hot component is not visible at bands 9 and 10 because they map lower layers, but it becomes pronounced for the lower receiver bands. The peak of the distribution reaches high temperatures at about 7 kK in band 3. This effect can also be seen in the QS region in the maps for higher receiver bands, which are dominated by cool areas and show only a few, less extended hot structures (cf. Figs. A.1–A.2).

In Fig. 4, the T_b distributions for band 3 and 6 are presented at different spatial resolutions corresponding to the original model grid spacing and to array configurations C1 to C7. The double-peaked QS distribution seen in the original resolution becomes less clear with decreasing resolution and tends toward a single-peaked more narrow distribution centered on the respective average value. In the FS and FP regions, the distributions also each tend toward a more narrow peak centered on the same average value.

The average value of the T_b distribution at the original resolution of band 3 is 6346 K in the QS region, 8606 K in the FS region, and 9635 K in the FP region. The average values of the T_b distributions for the degraded maps at resolutions corresponding to C1–C7 deviate by only 19 K in the QS region, 354 K in the FS region, and 270 K in the FP region at most from the average values at the original resolution. This result is expected because the spatial degradation smooths strong temperature

gradients that often occur over small and thus unresolved spatial scales, resulting in a narrower T_b distribution around roughly the same average value.

In band 6, the average values of the T_b distributions are at the original resolution 5254 K in the QS region, 6845 K in the FS region, and 7417 K in the FP region. The shift from these average values seen at the degraded resolutions (C1–C7) is even less in band 6 than in band 3 (Fig. 4) due to the smaller angular resolution (as set by the synthesized beam). In the vicinity of the selected QS region, the spatial scale and T_b distribution change little, so that the average value therefore remains the same even if it is sampled by a beam extending outside that region. However, in the immediate surroundings of the FS region lie the hot magnetic footpoint areas (including the FP region), which cause in a slightly higher average T_b with increasingly larger sampling beam. Similarly, the surroundings of the FP region are cooler on average than the FP region itself, resulting in a slightly lower average T_b with large sampling beams.

3.4. Spatial power distributions

The average spatial power spectra of the brightness temperature maps at the original resolution for the different receiver bands 3–10 are shown in Fig. 5a. The power spectra were calculated using radially averaged 2D fast Fourier transform (FFT) on the detrended (linear) brightness temperature maps over the entire FOV and averaged over the time range $t = 1550$ s–1750 s. The power at the larger scales ($\gtrsim 2''$) decreases with wavelength. This agrees with what is seen in the brightness temperature maps (Fig. 2), where band 6 exhibits less extended structures than band 3. This becomes even more notable by comparison with the T_b maps at shorter wavelengths of the upper receiver bands 9 and 10 (cf. Figs. A.1–A.2). Moreover, at the smallest scales, a few times the cell size of the model, the power for bands 9 and 10 is lower than for the lower bands.

The spatial power spectra of the degraded maps at resolutions corresponding to C1–C7 for bands 3 and 6 are presented in Figs. 5b–c. These power spectra are also averaged over the time range $t = 1550$ s–1750 s and over the entire FOV, as for the maps at the original resolution. In each panel, the corresponding minor and major axes of the synthesized beams are shown for reference.

The power at the degraded resolutions rapidly decreases at scales smaller than the corresponding synthesized beam. Consequently, a resolution corresponding to configuration C3 in band 6 is at the limit for adequately studying structures at subarcsecond scales. However, the power spectra clearly demonstrate the improvement for observations of small-scale dynamics that is provided with the higher angular resolution corresponding to array configuration C4 and above. For band 3, the array configuration C5 and above would be desirable for the same reasons. The reduction of the spatial power already starts at spatial scales larger than the clean-beam major axis. Depending on the scientific application, this is an important factor to consider.

3.5. Degradation of T_b excess signatures of dynamic events

An example of the time evolution of the brightness temperature of at a selected position in band 3 is presented in Fig. 6a at the original resolution and at resolutions corresponding to array configurations C1–C7. This illustrates the degradation of dynamic signatures due to limited angular resolution. This specific example is located in the QS region at $[x, y] = [-14''8, 13''1]$. The adapted selection criteria for brightening events are illustrated
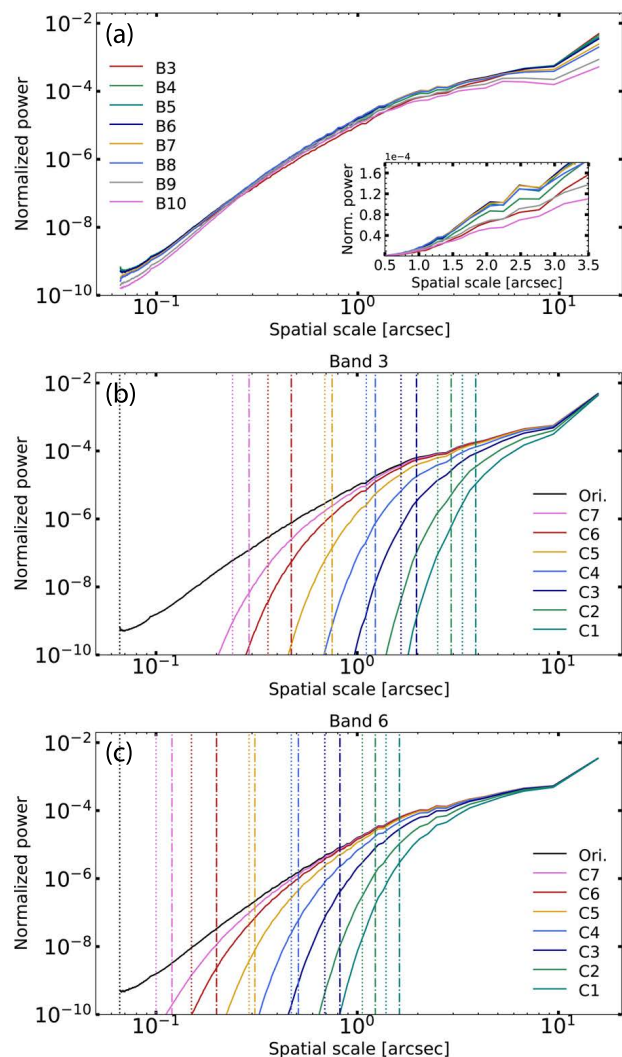

Fig. 5. Spatial power spectra. (*a*) Spatial power spectra of all bands at the original resolution, averaged over the entire FOV and between $t = 1550-1750$ s. The inset shows a zoom-in between spatial scales of $0.5-3.5$ arcsec, with the power on a linear scale. (*b*) and (*c*) Spatial power spectra of bands 3 and 6 at the original resolution and the resolutions corresponding to array configurations C1–C7 for each band. The FWHMs of the minor and major axes of the corresponding clean beams are marked with the vertical dotted and dot-dashed lines, respectively. For reference, the cell size of the numerical model (at 0.066 arcsec) is marked by the vertical dotted black lines.

in Fig. 6b, where the resulting ΔT_b is acquired by the difference between the peak temperature and the base temperature. To be on the conservative side, the base temperature of the specific event was defined as the hottest of the local pre- and post-minima. The peak, base, and minima temperatures are thus resolution dependent and were recalculated for each resolution. The peak centered on $t = 1140$ s (Fig. 6a) shows a T_b excess of over 3200 K with respect to the preceding minimum at the original resolution, but only approximately 290 K at the resolution of array configuration C3 and 240 K at C1. This corresponds to only about 9% and 7%, respectively, of the amplitude at the original resolution. The degree of the amplitude degradation of the dynamic signatures is dependent on the surrounding structures, which are sampled simultaneously with the clean beam. If a brightening event is well resolved, that is, if no other structure is mixed in within
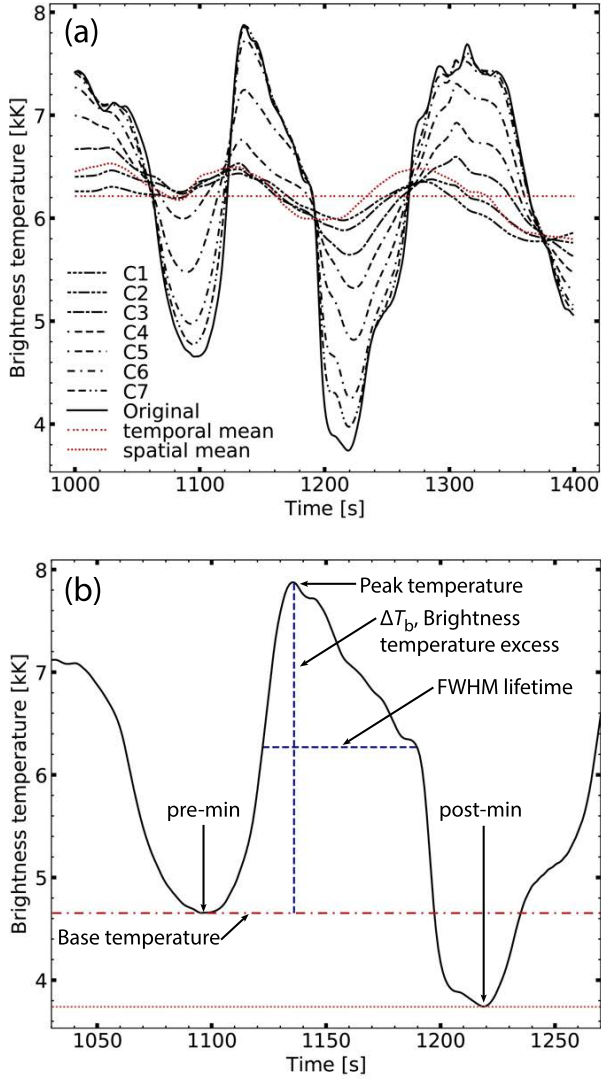
Fig. 6. Example of the degradation of T_b excess of a transient brightening event caused by limited spatial resolution and selection criteria for T_b excess. (*a*) The time evolution of the brightness temperature at $(x, y) = (-14''8, 13''1)$ in wavelengths of band 3 (cf. Table 1) is given for the map with original resolution (solid line) and for the spatially degraded maps corresponding to the respective array configuration. The dotted horizontal line marks the mean T_b value of the displayed time series at the original resolution, and the second dotted line shows the time evolution of the spatial mean value over a square of about 5 arcsecondse centered on the selected location. (*b*) Illustration of the selection criteria for the dynamic events. For each peak in the temporal evolution of the brightness temperature, the local pre- and post-minima are found. The base temperature for the specific event (horizontal dash-dotted red line) is defined as the temperature of the local minima with highest temperature, and the corresponding T_b excess of the event (vertical dashed blue line) is the difference between the peak temperature and the base temperature. The FWHM of the peak (horizontal dashed blue line) shows the lifetime of the brightening event.

the clean beam, the detectable amplitude of the event will be large. If a brightening event is not resolved separately from the surrounding "background" so that the potentially cooler "background" will be sampled by the same clean beam, then the resulting detectable amplitude of the brightening event will be reduced accordingly. Because the chromosphere contains structures at scales at the same order or even smaller than the angular reso-

lution of ALMA, the size and shape of the clean beam becomes an important factor. Figure 6 shows that with larger clean-beam size (smaller array configuration number), the magnitude of the dynamic T_b variations deviates less from the mean value of the surrounding area. For the same reasons that the hot brightening peaks are degraded in amplitude, the cool features would be observed as less cool (e.g., hotter) than they really are in the map at the original resolution. In this way, a small cool area in the original map can become nondetectable if there are dominant hot features in the vicinity that are sampled within the beam. For example, the cool signature around $t = 1100$ s in Fig. 6a is only weakly visible at the resolutions of C1–C3, and with temperatures close to or even above the mean value of the surrounding FOV or the temporal mean value at the selected location, a signature like this might be easily missed or disregarded in an analysis of data at low resolution.

An indication of the lifetime of the events is provided by the FWHM of the ΔT_b peak (Eklund et al. 2020). The lifetimes of the temperature excess typically are the same or even tend to be longer with lower resolution (see Sect. 4.4 for further discussion). More importantly, the specific time at which the temperature peak occurs can shift by up to a few tens of seconds (Fig. 6a). This causes variations in the small-scale dynamic signatures in the temporal domain. We discuss this in more detail in Sect. 3.6.

The time evolution of the brightness temperature is evaluated at all locations within the three different regions (QS, FS, and FP), between $t = 1000$–2000 s, at the original and degraded resolution. All instances of transient brightening events with $\Delta T_b > 20$ K are considered, well below what is reported for observed brightening events so far. In Fig. 7, the ΔT_b of all peaks at original resolution in receiver band 3 and 6 is plotted against the apparent T_b excess at lower angular resolutions, corresponding to the array configuration (C3) that has been used most frequently for solar observations so far. The correlations are illustrated by density distribution plots. Corresponding plots for combinations of other spatial resolutions for array configurations C1–C7 as well as for other frequencies corresponding to receiver bands 3–10 are provided in Appendix A.3.

There are brightening events with larger ΔT_b in the QS region than in the network regions FS or FP in both bands 3 and 6 (Fig. 7). Magnitudes of more than 6 kK are seen in the QS region in both bands, but only up to about 4 kK in the FS and FP regions. The distributions are quite broad, which results in substantial error bars for the conversion from (degraded) observed ΔT_b to the true (at the original resolution) ΔT_b value. This effect is more severe at lower resolution and is thus more evident at band 3 compared to band 6. The amplitudes of a majority of ΔT_b peaks at degraded resolution are underestimated. This is represented by the part of the distributions above the one-to-one ratio (indicated by the dotted lines in Fig. 7). Some brightening events exhibit a ΔT_b that is larger at the degraded resolution than at the original resolution. These cases are represented in the lower right corner in each of the distribution plots (Fig. 7), below the one-to-one ratio. This is specifically evident in the network regions (FS and FP) at the low resolution of band 3, where the most intense instances of ΔT_b seen at the degraded resolution actually correspond to relatively low ΔT_b at the original resolution. These ΔT_b increases mostly occur in the relatively cold areas (as seen at original resolution), which host additional nearby brightening events at distances within the same effective resolution element. These events are therefore no longer resolved individually. In these cases, a combined larger ΔT_b excess is observed. In some cases, depending on the surrounding dynamical structure, the
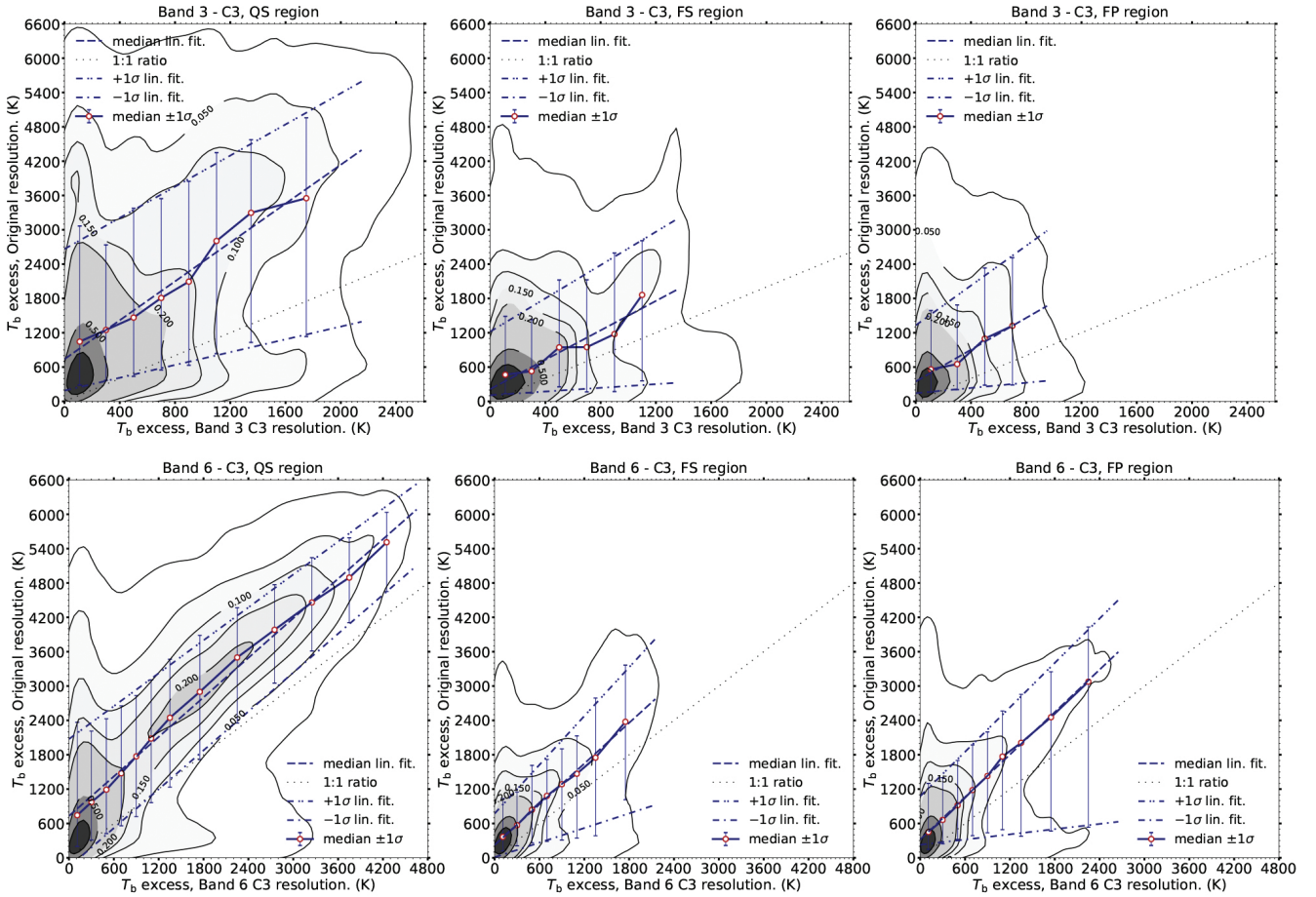
Fig. 7. Degradation of brightening events in band 3 (*top row*) and band 6 (*bottom row*), with the respective spatial resolution corresponding to array configuration C3. The T_b excess of brightening events at the original resolution plotted against the T_b excess at degraded resolution. The contour lines show the levels of 0.01, 0.05, 0.1, 0.15, 0.2, 0.5, and 0.75 of the density plot. The circles connected by the solid line show the median values (50th percentile) for the respective bin, and their error bars indicate plus and minus 1σ (e.g., 84th and 16th percentile). The dashed line marks a linear fit to the median values, and the dash-dotted lines mark linear fits to the $\pm 1\sigma$ values. The dotted line marks the ratio of one-to-one for reference.

resulting ΔT_b at the degraded resolution can be on the order of up to a few thousand K, while the peak values at the original resolution only reach a few hundred K, as indicated in Fig. 7. For these reasons, the choice of specific locations for an in-depth analysis of observational data is very important. For example, the brightest point of a brightening event will be underestimated and the surrounding cooler parts of the "background" will be overestimated, while the most accurate temperature is sampled somewhere in between.

The distributions of the $\Delta T_{b,deg}$ at the degraded resolution as a function of $\Delta T_{b,org}$ at the original resolution allow us to estimate the typical degradation of ΔT_b for the different types of regions considered here. The degradation factors could then in principle be applied inversely, as correction factors to observational data of similar regions. We show below, however, that these correction factors have significant error bars. In order to derive the typical impact on the reduced angular resolution on the simulated ΔT_b amplitudes, the median and standard deviation values were calculated in the bins at degraded resolution of $\{0.02 - 0.2, 0.2 - 0.4, 0.4 - 0.6, 0.6 - 0.8, 0.8 - 1.0, 1.0 - 1.2, 1.2 - 1.5, 1.5 - 2.0\}$ kK, with continuation upward of bins with a width of 0.5 kK. In most cases, the median values and the plus/minus one standard deviation values can be reasonably well estimated by a

linear fit (see Fig. 7). The relation between the T_b excess of the dynamic signatures at the original ($\Delta T_{b,org}$ [kK]) and degraded ($\Delta T_{b,deg}$ [kK]) resolution can thus be approximated as

$$\Delta T_{b,org} = \kappa(\nu, C)\,\Delta T_{b,deg} + \mu(\nu, C), \tag{3}$$

where κ and μ are variables that depend on the frequency ν (and thus on receiver band) and array configuration C (and thus on the diameter of the synthesized telescope aperture). The values of κ and μ for each combination of receiver bands 3–10 and array configurations C1–C7 are given in Fig. 8 for the median values and plus/minus one standard deviation. The underlying density plots are provided in Appendix A.3 for clarity and allow more accurate direct applications because they entail more detailed information than the approximated linear functions. The accuracy of the translation from observed (degraded) ΔT_b to true (fully resolved) ΔT_b for dynamic brightening events in the different characteristic regions (QS, FS, and FP) at the frequencies of the spectral bands 3–10 at the respective resolution corresponding to array configurations C1–C7 can thus be acquired from Fig. 8. The grid cell resolution of the employed numerical model limits this study to array configurations C6 for band 8 and C5 for bands 9 and 10. As mentioned above, there
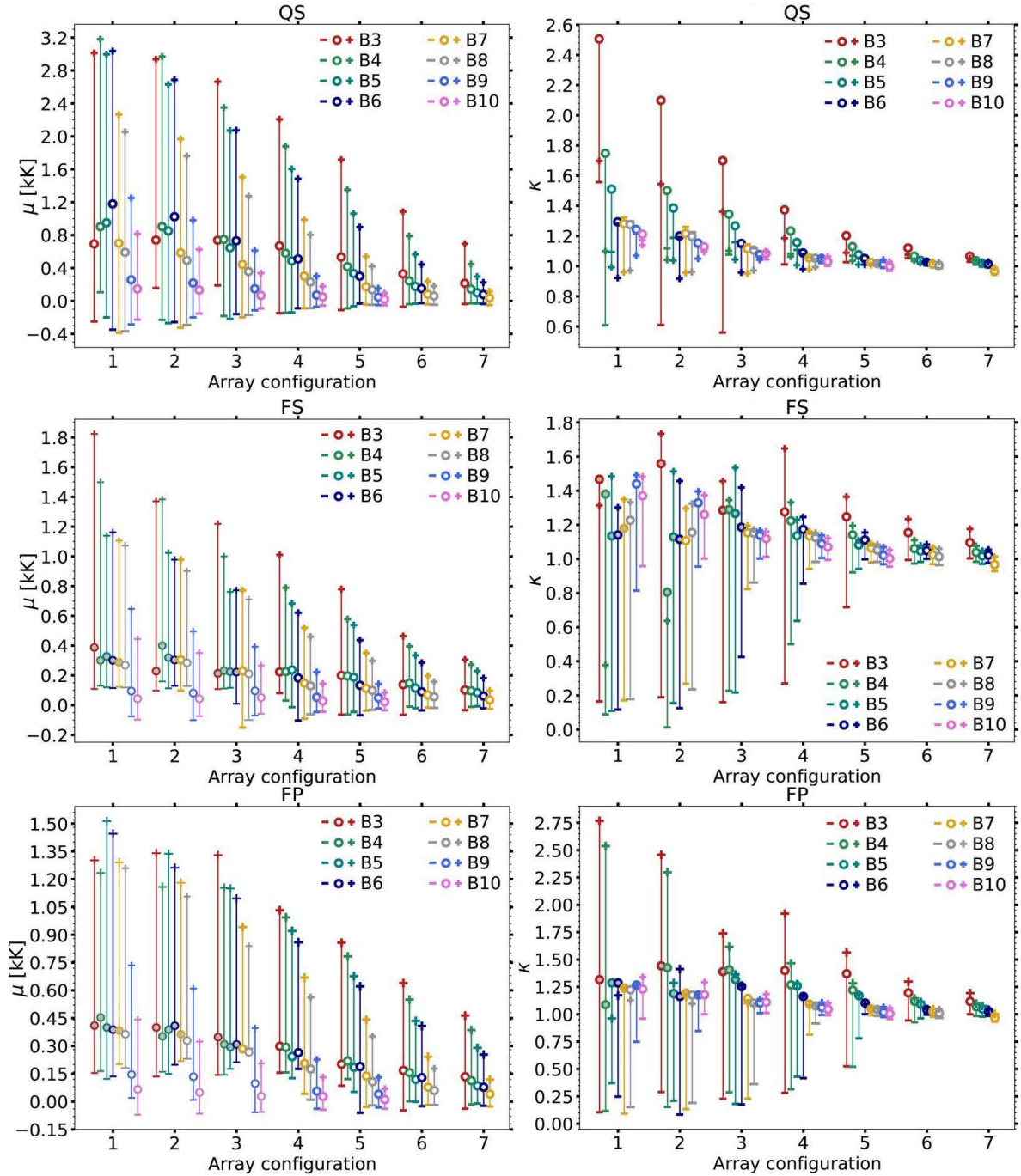
Fig. 8. Parameters of linear fits for Eq. (3) to the brightness temperature excess density plots (as in Fig. 7). All combinations of spectral bands 3–10 and array configurations C1–C7 are given for the three selected regions, QS (*upper row*), FS (*middle row*), and FP (*bottom row*). The linear fits across the bins to the median values are indicated by the circles and to plus and minus one standard deviation are marked with plus and minus signs, respectively. *Left column*: μ, indicates the scalar shift of T_b, and the *right column*, κ, indicates the slope of the linear fit. The cases in which the most intense brightening instances are dominated by apparent brightening are marked with filled gray circles.

areat certain combinations of receiver bands and array configurations, primarily corresponding to low resolution, the features with the largest ΔT_b in the maps at the degraded resolution have no strong ΔT_b counterpart at the original resolution. This is most relevant in the FS and FP regions with the lower resolutions, see for example the brightest events at the degraded resolution in the FS or FP regions of band 3 in Fig. 7. These events might be misinterpreted. These cases are marked with gray circles in Fig. 8. The values in Fig. 8 are corrected for this and do not account for the distribution of the most bright apparent events. This means

that only ΔT_b up to where the strongest events at the degraded resolution have a strong counterpart at the original resolution are considered in each case. This can be seen in detail in the distribution plots for all combinations of receiver bands and array configurations in Appendix A.3. By comparing the distributions with increasing resolution, it becomes clear at which resolution these events that appear to be most bright disappear.

For example, for an event detected in the QS region in band 3 at the degraded resolution corresponding to array configuration C3, with an amplitude of the brightness temperature excess of

1.2 kK, Fig. 8 indicates $\mu = 0.74$ and $\kappa = 1.7$ for the median values and for the $\pm 1\sigma$; $\mu_{-\sigma} = -0.19$, $\mu_{+\sigma} = 2.66$ kK, $\kappa_{-\sigma} = -0.56$, and $\kappa_{+\sigma} = +1.36$. Inserting these values into Eq. (3) separately for the median and $\pm 1\sigma$, respectively, yields a span of corresponding amplitudes at the original resolution between 0.86 kK to 4.29 kK with a median value of 2.78 kK, that is, a resulting estimated temperature of $T_{\text{b,ori}} = 2.78^{+1.51}_{-1.92}$ kK.

It is important to note is that as the spreads of the distributions are large already with the presented values in Fig. 8, which only represents the values within one standard deviation, taking into account two or even three standard deviations would in some cases give rise to more than twice the span of the distribution. The high degeneracy naturally comes from the lack of information about how well resolved the events are in the spatially degraded data. For this reason, the distributions are not intended for performing one-to-one corrections of specific events in observational data. The results we present here instead provide an estimation of the expected uncertainties that should be accounted for when the magnitudes of brightening events in observational data are analyzed.

In conclusion, a resolution as high as possible should be used to measure the magnitudes of small-scale brightening events because it reduces the uncertainty in the conversion to the true brightness temperature excess. In particular, using array configuration C4 instead of configurations C1–C3 for band 3 observations that has been frequently used so far would greatly reduce these uncertainties. For instance, the example above with $\Delta T_{\text{b}} = 1.2$ kK has a corrected median value of 2.28 kK for C4 instead of the 2.78 kK for C3, which is 0.5 kK smaller and corresponds to a reduction of 0.42 times the measured ΔT_{b}. The spread between $\pm 1\sigma$ is reduced from 3.43 kK at C3 to 2.52 kK at C4, which is a difference of 0.91 kK or 0.76 times the measured ΔT_{b}.

3.6. Temporal power distributions

As indicated in the example in Fig. 6, the appearance of the temporal T_{b} variations at specific locations is dependent on the surrounding spatial structures that lie within the effective resolution element. In this sense, the temporal and spatial variations are connected. The effect of limited spatial resolution is thus important when T_{b} variations in the temporal domain are studied. As a means to inspect the effect of degraded spatial resolution on oscillatory signals, the temporal power spectra were calculated at all individual pixels over the entire time span of the simulation ($t = 0$ s–3460 s) and averaged over the FOV in the respective regions. Prior to the Fourier analysis, each signal was detrended (linearly) and apodized using a tapered cosine window (Harris 1978). The temporal power spectra are shown for band 3 and band 6 for the three selected regions in Fig. 9.

For the QS region, the power spectra for both bands 3 and 6 show enhanced power at periods around 180 s with secondary peaks at approximately 150 s, 200 s, and 260 s. There are also significant enhancements at 350 s and 500 s, although they are more evident in band 3 than in band 6.0 The dominating peak around 180 s agrees well with the 3 min oscillatory behavior seen in quiet-Sun regions at chromospheric heights in observations (see, e.g., Jafarzadeh et al. 2021, and references therein) and also simulations (e.g., Wedemeyer et al. 2004). The peak at 180 s is also well represented in the power spectra for the degraded maps at lower spatial resolution, even at the lowest resolution of C1 in both bands, although with reduced power at all periods. The power of the secondary peak at 150 s is slightly less reduced with decreasing resolution for both receiver bands as compared to the primary peak. As a result, the peak at 150 s appears dominant at

a resolution corresponding to array configuration C1. The peaks at longer periods, 260 s, 350 s, and 500 s, instead appear less pronounced at lower spatial resolution and are barely discernible at C1 for either bands 3 and 6.

In the network regions, FS and FP, the power increases with period for bands 3 and 6 due to notable temperature variations on long timescales in the numerical model in connection with the evolution of the magnetic topology. The power at longer periods (>500 s) is reduced more significantly with degraded resolution compared to those with periods shorter than 500 s. The integrated power over all periods is highest for the QS region, followed by the FP region, and it is lowest for the FS region. The integrated power is roughly one order of magnitude lower with the degraded spatial resolution of C1 compared to the original resolution for each of the selected regions. In the FS region, at band 3, there is a power enhancement at periods between roughly 400 s to 500 s, which becomes more prominent at lower resolution. For band 6 in the FS region, there are no clear enhancements, but only some indications around 250 s and 350 s, which appear stronger with higher spatial resolution. As indicated in Sect. 3.2, band 3 mostly samples the magnetic loop structures in the FS region, while band 6 also partly samples lower heights, which could suggest that the enhancement at 500 s in band 3 originates from the magnetic field loops. The magnetic footpoint region FP shows modest enhancements at short periods around 200 s and 310 s in both bands 3 and 6 at the original resolution. As a result of the reduced power at long periods for lower spatial resolution, the enhancements appear more pronounced.

4. Discussion

4.1. Numerical model

The Bifrost model provides a realistic test case because it exhibits a substantial span of spatial and temporal scales and also combines characteristic regions from quiet Sun (QS) to magnetic field footpoints (FP; Fig. 2). For these reasons, models with the same setup have been used for the study of other synthetic chromospheric observables (e.g., Pereira et al. 2015). The results of this work can thus be transferred to observations of solar targets that probably show comparable conditions of the observables, as seen in any of the selected targets, such as a similar magnetic field strength and topology and similar spatial scales and contrasts.

Dynamics at small spatial scales are often also correlated with short timescales as a direct consequence of finite velocities. In the QS region, for instance, the pattern of propagating shock fronts shows typical scales up to several arcseconds and timescales of several tens of seconds (Eklund et al. 2020, 2021; Wedemeyer-Böhm et al. 2007). Long-term variations in the numerical model are connected to the evolution of the magnetic field topology as a result of the simulated magnetoconvection.

The magnetic field topology in the FS region of the employed 3D model is also useful for studying the effects of limited spatial resolution on mm observations of narrow magnetic loops (see Sect. 3.3). In particular for the lowest resolution cases discussed here (e.g., C1-C3 of band 3), caution should to be taken when observational results are interpreted because the relatively large synthesised beams result in a mixing of the magnetic field structure and its immediate surroundings. The same applies to all observations of features with spatial extents at or below the effective spatial resolution (see Sect. 3.5).
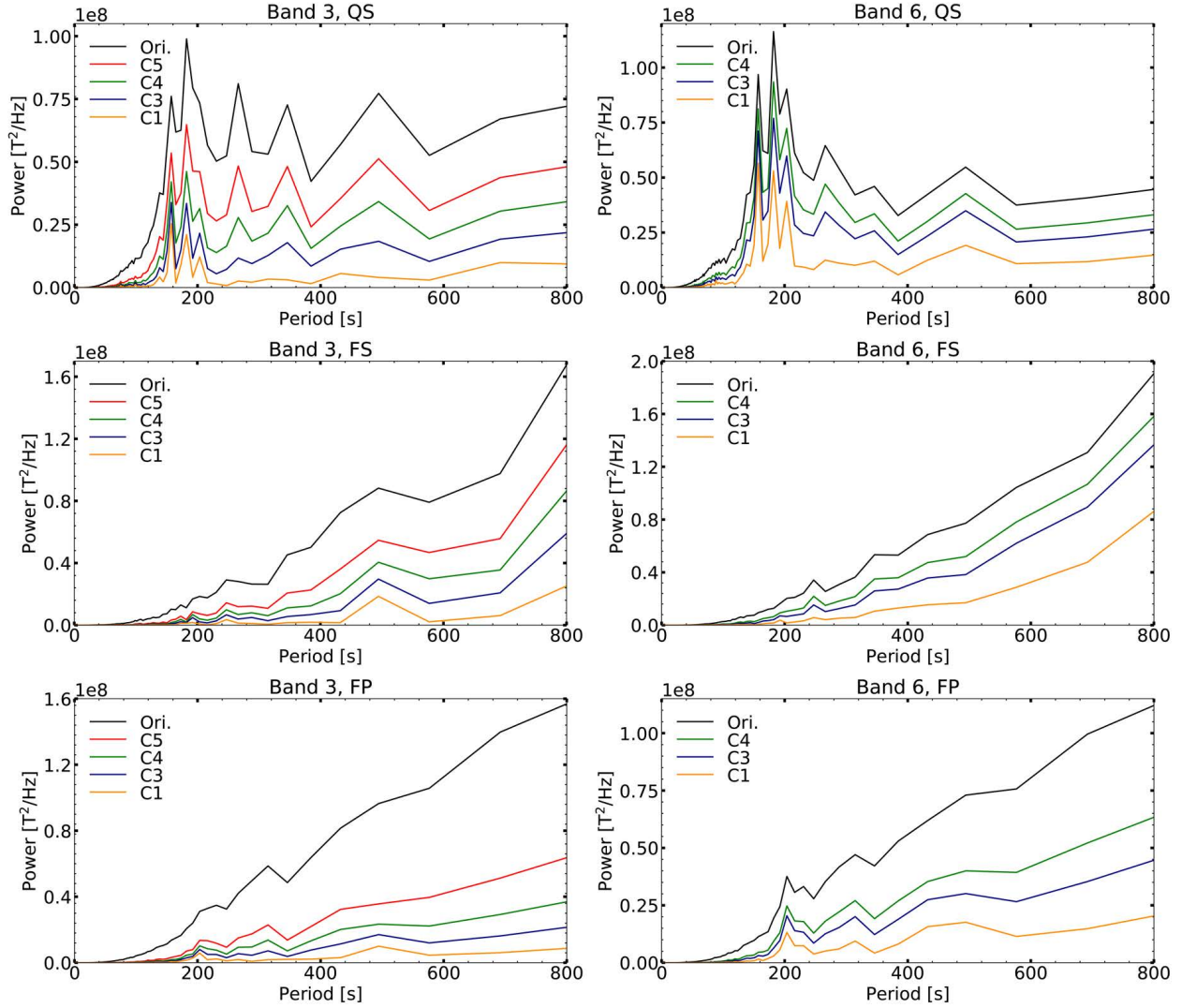
Fig. 9. Temporal power spectra of bands 3 (*left column*) and 6 (*right column*) at the three characteristically different regions (cf. Fig. 2). *Upper row*: QS region. *Middle row*: FS region. *Bottom row*: FP region. The spectra are calculated at the original resolution and at the resolutions corresponding to array configurations C1, C3, C4, and C5 for band 3 and C1, C3, and C4 for band 6, and they represent mean values over the FOV within each region.

4.2. Imaging with ALMA

As a first step, the method we chose represents a best-case scenario with optimal observing conditions. In reality, there are additional limitations and sources of uncertainties such as instrumental noise and the Earth's atmosphere that impact observations, especially those of small-scale dynamics. More extensive modeling is required to take these effects properly into account. This is currently limited by our incomplete knowledge of the atmosphere above the ALMA site during daytime (solar) observations. Furthermore, interferometric observations sample the target only at certain spatial scales and certain angles as determined by the so-called baselines of the interferometric array. Each baseline connects two antennas in the array and measures one spatial Fourier component of the target source. The longest baselines determine the minimum resolvable scales (cf. Table A.2), but are also more affected by atmospheric disturbances. Improving the spatial resolution by means of extending the interferometric array therefore comes with challenges related to the required correction of atmospheric disturbances. To which degree it is feasible to perform reliable solar observa-

tions in more extended array configurations needs further studies and considerations. Here, it is important to note that the magnitude of the corresponding uncertainties in the final images depends on the wavelength. Typically, the longer the wavelength (the lower the receiver band number), the less affected the interferometric observation by uncertainties arising from variations in the atmosphere above the telescopes. In addition, it is possible that uncertainties and artifacts are introduced to the data through post-processing procedures. For instance, the removal of PSF sidelobes in the initial 'dirty image' can have a very strong effect on the resulting 'clean image'. The most commonly used deconvolver algorithm for this, the CLEAN algorithm (Högbom 1974), treats the target as a collection of point sources and is suboptimal for extended targets on the Sun through its inherited nature. Consequently, the imaging and post-processing in general should be reviewed and adopted for solar observations in the future. The detailed modeling of an interferometric observation of the Sun with ALMA would require the production of artificial measurement sets, application of instrumental and atmospheric noise, and subsequent imaging. This computationally expensive approach would blend the effect of the overall angular resolution

with the specifics of the employed imaging algorithm and the assumed noise properties. We therefore restrict this first study to the more straightforward convolution of synthetic mm maps with the synthesized beam, that is, the main beam of the PSF corresponding to the considered combination of receiver band and array configuration.

While the effects described above certainly affect the quality and therefore the scientific value of the observational data, the limited spatial resolution that we addressed in this study has a major effect on the observables and the signatures correlated to the small-scale dynamics. The results presented here demonstrate that it is favorable to perform observations with a spatial resolution as high as possible, which would require the commissioning and usage of wider array configurations for solar observing. To which degree this will result in an improvement ALMA observations of small-scale features ultimately depends on the handling of the effect of the Earth's atmosphere on the longest baselines and appropriate imaging strategies.

4.3. Eccentricity of clean beams

A very important effect attached to the interferometric observations is the size and shape of the clean beam. The size and shape can vary when antennas are removed from the measurement set in the calibration stage, for instance, which is essentially equivalent to modifying the antenna configuration. However, the size and shape of the clean beam unavoidably varies in time because the angle of the target on the sky changes and thus depends on the time of the day. At short timescales within an observation, the sizes of the clean-beam axes typically vary by about a few percent only (Wedemeyer et al. 2020), but this also depends on the time of the day with more rapid variations as the target recedes from zenith.

In this study, the clean beams were kept static and slightly eccentric (cf. Table A.2), which represents more optimal conditions in which the Sun is located high on the sky. In Fig. 10, the variations in size and eccentricity of the clean beam with the time of the day are given, with the standard case of the study as reference ($t = 0$ min). The clean-beam minor axis remains fairly constant in comparison to the major axis, which roughly doubles in size over the course of a few hours. The size of the clean beam plays an imperative role in the ability to resolve the small-scale structures and to the appearance of dynamic features. In addition, it is also very important to consider the shape (eccentricity) and orientation (position angle) of the clean beam in the analysis of observational data. With a highly eccentric beam shape and thus a corresponding resolution element, the small-scale structures are differently resolved in different directions. Figure 10 shows that the resolution is higher in the direction along the minor axis of the clean beam. For this reason, the orientation (position angle) of the clean beam becomes increasingly important with higher eccentricity and thus for solar observations taken early or late in the day.

In this first study, the position angle was set to a constant value (of 80 degrees, Table A.2) to enable one-to-one comparisons between the different cases. Although the resolution is relatively high along the clean-beam minor axis, the dynamics and structures on small spatial scales are still affected by larger spatial sampling in the perpendicular direction, along the major axis. In this sense, to be on the conservative side in the data analysis, the effects that an extended resolution element has on the appearance of small-scale dynamics can be estimated by matching the major axis to the beam sizes given in this work. We determined that an extensive study with more eccentric clean beams would
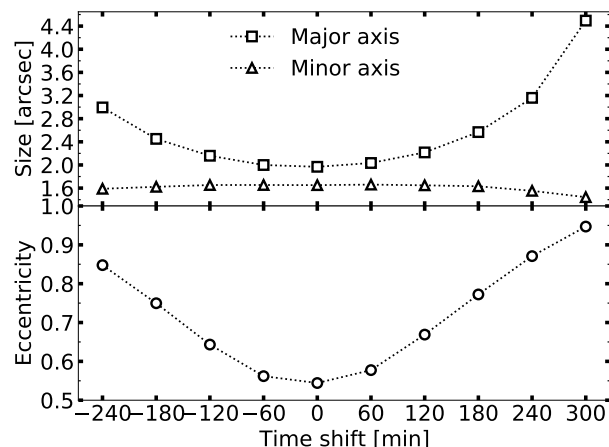

Fig. 10. Clean-beam size (*a*) and eccentricity (*b*) with varying time on the day. The example illustrates band 3 at array configuration C3, and the *x*-axis indicates the time shift from the standard case (close to circular clean beam) we used in our analysis.

be too excessive to be included in the present work, and this remains a subject for a potentially forthcoming publication.

4.4. Comparison with observations

The dependence of the observable signatures of the dynamic small-scale structure at ALMA wavelengths on the angular resolution agrees well with what is seen in studies of observational data. In the network regions (FS and FP), the maximum T_b excess of the dynamic signatures is lower than in the QS region (Fig. 5). This is in line with the results from the analysis of observational band 3 data (taken in configuration C3) by Eklund et al. (2020). The reported resolution is comparable to the band 3 C3 values in this study (see Fig. 1). Eklund et al. (2020) also reported detection of events with substantial ΔT_b less frequently in areas with relatively higher magnetic field strengths, which agrees with the results presented in this study (see Sect. 3.5). The distributions of the observed ΔT_b of the brightening events reported in Eklund et al. (2020) are shown in Fig. 11 for the network (NW) and inter network (INW) regions separately (see Eklund et al. (2020) for details). Equation (3) is applied to the ΔT_b of the brightening events with values κ and μ (Fig 8) for band 3 in array configuration C3. The QS values are used for the events observed in the INW regions and the FS values for the events observed in the NW region. The peak of the resulting distribution of corrected ΔT_b is shifted by about 1000 K from around 650 K to 1750 K for the INW events and about 400 K from around 550 K to 950 K for the NW events. However, the extent of the $\pm 1\sigma$ range of the corrected ΔT_b values is large. In Eklund et al. (2020), only events with $\Delta T_b > 400$ K were considered for the detection of the brightening events, to be on the conservative side in view of the noise level in the data.

The lower limit of ΔT_b for detecting brightening signatures is dependent on the level of noise in the data. The effect of reduced spatial resolution presented in this study (Sect. 3.5) could however be used to estimate the reliability of the detected brightening events. At reduced resolution, the magnitudes of the T_b excess are suppressed (Figs. 7–8), while there is a more linear distribution between the lifetimes of the events at degraded and original resolutions (Fig. 12a). For this reason, shock signatures that show a relatively small T_b excess in observations with low angular resolution should still show a lifetime that is in line with what
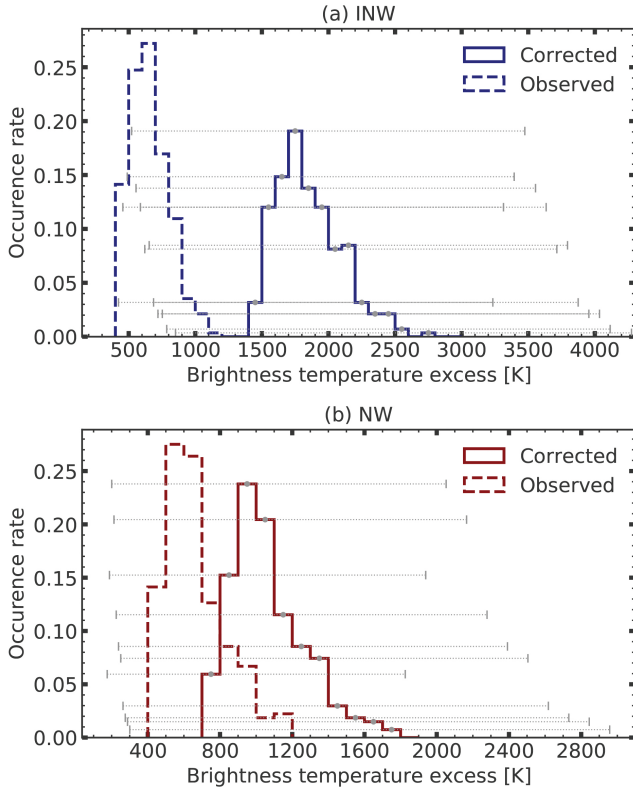
(a) INW

(b) NW

Fig. 11. Distributions of ΔT_b of observational brightening events from Eklund et al. (2020) with their corrected ΔT_b according to Eq. (3) and Fig. 8. (a) The events observed within the INW regions (dashed blue) along with the estimated distribution using the values for QS region derived here (solid blue), with bars showing $\pm 1\sigma$ for each bin. (b) The observed events in the NW regions (dashed red) and the corrected distribution using the values for the FS region, with the indications of $\pm 1\sigma$ for each bin.
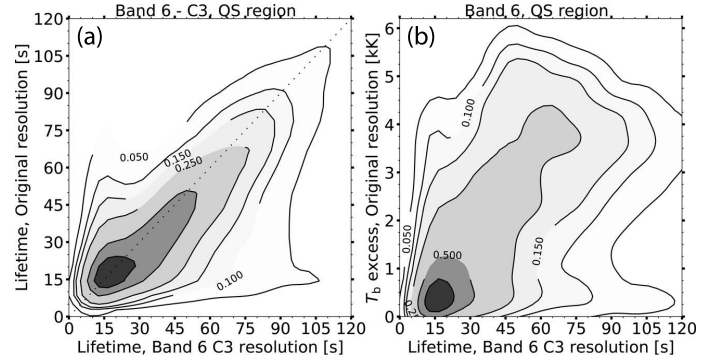

Fig. 12. Lifetimes of transient brightenings in the QS region at band 6. (a) Lifetimes at original resolution vs. lifetimes at degraded resolution corresponding to array configuration C3. (b) Brightness temperature excess at original resolution vs. lifetimes at degraded resolution corresponding to array configuration C3. The levels of the density plot, 0.05, 0.1, 0.15, 0.25, 0.5, and 0.75, are marked by the contour lines.

loops reported by Wedemeyer et al. (2020), which may be comparable to the loops represented in the simulation model used in this study. The analysis of Jafarzadeh et al. (2021) shows that in regions with larger magnetic field strength, with overlying loops or footpoints, the resulting dominating periods are longer than in the more quiet regions. This agrees with the periods seen in the current result of the FP region and the FS region at the resolution of C3 (Fig. 9).

4.5. Comparison with previous studies of synthetic observables

Synthetic brightness temperatures of radiation at mm wavelengths from 3D numerical models of the quiet Sun have previously been calculated for example by Wedemeyer-Böhm et al. (2007) and Loukitcheva et al. (2015). A nonmagnetic model (Wedemeyer et al. 2004) was used by Wedemeyer-Böhm et al. (2007), who reported resulting quiet-Sun brightness temperature distributions at 1.0 mm and 3.0 mm with average values of 4.7 kK and 4.9 kK, respectively. The corresponding simulated values that we find in the current work (about 5.3 kK at 1.2 mm and 6.3 kK at 3.0 mm; see Fig. 4) are slightly higher, possibly as a result of the inclusion of magnetic fields in the Bifrost model. Wedemeyer-Böhm et al. (2007) reported T_b distributions at 1.0 mm and 3.0 mm, with double-peaked characteristics as a result of sampling the cool background and hot shocks, which agrees with what we see in the current work (Fig. 4). Loukitcheva et al. (2015) used the same publicly available Bifrost-enhanced network model as we used in the current work (see Sect. 2). Based on one snapshot, Loukitcheva et al. reported average brightness temperatures over the entire FOV of 4.8 kK at 1.0 mm and 6.1 kK at 3.0 mm. The values averaged over the ALMA bands of the current work agree well with these values, but are slightly higher because slightly longer wavelengths were included in both cases.

The angular resolution necessary to resolve the chromospheric shock-wave-induced mesh-like pattern was estimated by Wedemeyer-Böhm et al. (2007) by degrading a synthetic mm map at 1.0 mm to resolutions between 0.3 arcsec and 0.9 arcsec. With a resolution of 0.9 arcsec, the finest structures remain unresolved, but the larger pattern is visible. Loukitcheva et al. (2015) also estimated the effect of spatial smearing by degrading the synthetic mm maps from the Bifrost snapshot to resolutions of 0.2, 0.4, 1.0, and 4.0 arcsec, respectively. They concluded

is seen in the original resolution. Detection of transient brightening events with modest T_b excess in comparison to the surrounding average temperature has been reported. For instance, Nindos et al. (2020) reported events with $\Delta T_b \approx 70$ K in band 3 data with an eccentric clean-beam size of 2.5 arcsec×4.5 arcsec. The high eccentricity of the clean beam gives rise to larger uncertainties, as discussed in Sect. 4.3. This resolution is at best (along the minor axis) comparable with array configuration C2 of band 3, as indicated in Fig. 1. Correlating these modest ΔT_b signatures with their respective lifetimes could bring further insights into their origin and assist in sorting out signatures that might be due to noise or similar. For example, for a propagating shock wave, the lifetime is several tens of seconds (Eklund et al. 2021, 2020) with a general trend of increasing lifetime with increasing ΔT_b, as indicated in Fig. 12b.

The repetitiveness of dynamic events in ALMA band 3 data of a QS region with some network patches was derived by Eklund et al. (2020), where a dominating period of around 200 s, with well-represented periods up to 320 s and declining representation up to about 430 s, was reported. This agrees very well with what is seen here in the QS region of the synthetic mm maps (Fig. 9). Their analysis was restricted to the central parts of the FOV, including the most quiet parts, but similar calculations of oscillations were made for a larger FOV by Jafarzadeh et al. (2021), where structures with stronger magnetic field strength were included, such as the compact magnetic magnetic field

similarly to Wedemeyer-Böhm et al. (2007) that a resolution of up to 1.0 arcsec is adequate for observations of the chromospheric small-scale structure. As shown in the current work, this is achieved by observations in array configuration C3 at band 6 and C5 at band 3, for instance.

The average formation heights reported by Wedemeyer-Böhm et al. (2007) are about 0.77 Mm and 0.99 Mm for radiation at 1 mm and 3 mm, respectively. These values are significantly lower than the average values of the QS region in the current work, 0.93 Mm (at 1.2 mm) and 1.36 Mm (at 3 mm). One contributing factor to this might be the lack of a transition region in the model by Wedemeyer-Böhm et al. (2007). Previous work on dynamic 1D models by Loukitcheva et al. (2004) shows that for some propagating shocks, radiation at 1 mm and 3 mm can form very close to the transition region. However, as concluded in Eklund et al. (2020), it is important to take the inhomogeneous structure of the 3D atmosphere into account when dynamic small-scale features are studied.

Martínez-Sykora et al. (2020) calculated synthetic observables at 1.2 mm and 3.0 mm based on a 2D numerical model including ambipolar diffusion (Martínez-Sykora et al. 2012, 2017), for which they reported average radiation formation heights of 2.7 Mm at 1.2 mm and 2.8 Mm at 3.0 mm, which suggests that ALMA bands 3 and 6 forms at similar heights. While the implemented modeling of relevant processes is certainly an improvement over previous modeling attempts, it is not clear whether it compensates for the restriction to two spatial dimensions. In this regard, it should be stressed that it is important to model the dynamic small-scale structure of the chromosphere in full 3D. Further studies are therefore needed in order to better understand the achieved degree of realism of the different models. For instance, comparison of observations at similar angular resolution at bands 3 and 6 of the same features, for example, magnetic field loops as reported in Wedemeyer et al. (2020) (where the results of this work for the FS and FP regions can be applied), might reveal whether the two bands show a high correlation and form at similar heights.

5. Conclusion

Choosing the correct combination of array configuration and receiver band is essential in view of the requirements of a set science goal because it determines the achievable spatial resolution. The predictions presented here, based on state-of-the-art simulations, clearly demonstrate that this is in particular important for the study of small-scale features. The amplitudes of brightness temperature signatures of transient brightening events, such as propagating shock waves, are severely reduced at low spatial resolution (Fig. 7), which is typically given at a compact array configuration, for example, C1–C3 for band 3 or C1–C2 at frequencies corresponding to up to band 7. Moreover, as a result of low spatial resolution, the exact time at which a temperature peak occurs can be shifted by up to a few tens of seconds with respect to the fully resolved case (Fig. 6a) because temporal and spatial scales tend to be coupled. For this reason, the observed oscillatory behavior as seen in temporal power spectra is also affected by the spatial resolution, which means that certain ranges of oscillation periods appear to be more prominently than they would be at full resolution (Fig. 9).

The radiation mapped by the different ALMA receiver bands originates at different heights that range from the low chromosphere for the highest numbered receiver bands to the high chromosphere for the lowest numbered bands. The average for-

mation height increases with wavelength from 0.6 Mm at band 10, to 0.9 Mm at band 6 to 1.3 Mm at band 3 in the simulated QS region. In the presence of magnetic field loops (FS region), the formation heights for the lower bands increase and reach an average value of up to 1.9 Mm at band 3, with small contributions from as high as 2.5–3.0 Mm. We note that (i) the distribution of the formation heights of the different bands displays several components (Fig. 3) and (ii) the formation height varies substantially in both location and time. The variations at one receiver band are on the same order or even larger than the typical differences of formation heights between the receiver bands, resulting in large overlaps that should be taken into account when relative differences between the receiver bands are studied.

Our simulations demonstrate the scientific potential of the solar observing capabilities currently provided by ALMA and how simulations can aid the in-depth analysis of observations, for instance, by providing correction factors for brightness temperature amplitudes of small-scale transient events. The overall conclusion is that a high spatial resolution, which is essential for studies of the dynamic small-structure of the solar chromosphere, can in principle be achieved with wider array configurations of ALMA. In order to unlock the full potential of solar observing with ALMA, further development of observing strategies and imaging procedures is required.

References

Bello González, N., Flores Soriano, M., Kneer, F., & Okunev, O. 2009, A&A, 508, 941
Bello González, N., Franz, M., Martínez Pillet, V., et al. 2010, ApJ, 723, L134
Borrero, J. M., Jafarzadeh, S., Schüssler, M., & Solanki, S. K. 2017, Space Sci. Rev., 210, 275
Carlsson, M., Hansteen, V. H., Gudiksen, B. V., Leenaarts, J., & De Pontieu, B. 2016, A&A, 585, A4
Chintzoglou, G., De Pontieu, B., Martínez-Sykora, J., et al. 2021a, ApJ, 906, 82
Chintzoglou, G., De Pontieu, B., Martínez-Sykora, J., et al. 2021b, ApJ, 906, 83
da Silva Santos, J. M., de la Cruz Rodríguez, J., Leenaarts, J., et al. 2020, A&A, 634, A56
de la Cruz Rodríguez, J., Szydlarski, M., & Wedemeyer, S. 2021, ART: Advanced (and fast!) Radiative Transfer code for Solar Physics, https://github.com/SolarAlma/ART
Eklund, H., Wedemeyer, S., Szydlarski, M., Jafarzadeh, S., & Guevara Gómez, J. C. 2020, A&A, 644, A152
Eklund, H., Wedemeyer, S., Snow, B., et al. 2021, Phil. Trans. R. Soc. London Ser. A, 379, 20200185
Gafeira, R., Lagg, A., Solanki, S. K., et al. 2017, ApJS, 229, 6
Gudiksen, B. V., Carlsson, M., Hansteen, V. H., et al. 2011, A&A, 531, A154
Guevara Gómez, J. C., Jafarzadeh, S., Wedemeyer, S., et al. 2021, Phil. Trans. R. Soc. London Ser. A, 379, 20200184
Harris, F. J. 1978, IEEE Proc., 66, 51
Högbom, J. A. 1974, A&AS, 15, 417
Jafarzadeh, S., Rutten, R. J., Solanki, S. K., et al. 2017, ApJS, 229, 11
Jafarzadeh, S., Wedemeyer, S., Fleck, B., et al. 2021, Phil. Trans. R. Soc. A Math., 379, 20200174

Jafarzadeh, S., Wedemeyer, S., Szydlarski, M., et al. 2019, A&A, 622, A150
Jess, D. B., Snow, B., Fleck, B., Stangalini, M., & Jafarzadeh, S. 2021a, Nat. Astron., 5, 5
Jess, D. B., Jafarzadeh, S., Keys, P. H., Stangalini, M., & Verth, G. 2021b, lrsp, submitted
Loukitcheva, M., Solanki, S. K., Carlsson, M., & Stein, R. F. 2004, A&A, 419, 747
Loukitcheva, M., Solanki, S. K., & White, S. 2006, A&A, 456, 713
Loukitcheva, M., Solanki, S. K., Carlsson, M., & White, S. M. 2015, A&A, 575, A15
Loukitcheva, M., White, S. M., Solanki, S. K., Fleishman, G. D., & Carlsson, M. 2017, A&A, 601, A43
Martínez-Sykora, J., De Pontieu, B., & Hansteen, V. 2012, ApJ, 753, 161
Martínez-Sykora, J., De Pontieu, B., Carlsson, M., et al. 2017, ApJ, 847, 36
Martínez-Sykora, J., De Pontieu, B., de la Cruz Rodriguez, J., & Chintzoglou, G. 2020, ApJ, 891, L8
Molnar, M. E., Reardon, K. P., Chai, Y., et al. 2019, ApJ, 881, 99
Nindos, A., Alissandrakis, C. E., Bastian, T. S., et al. 2018, A&A, 619, L6
Nindos, A., Alissandrakis, C. E., Patsourakos, S., & Bastian, T. S. 2020, A&A, 638, A62
Patsourakos, S., Alissandrakis, C. E., Nindos, A., & Bastian, T. S. 2020, A&A, 634, A86

Pereira, T. M. D., Carlsson, M., De Pontieu, B., & Hansteen, V. 2015, ApJ, 806, 14
Remijan, A., Biggs, A., Cortes, P., et al. 2020, ALMA Doc., 8.3, ver. 1.0, 8.3
Rodger, A. S., Labrosse, N., Wedemeyer, S., et al. 2019, ApJ, 875, 163
Rouppe van der Voort, L., Leenaarts, J., de Pontieu, B., Carlsson, M., & Vissers, G. 2009, ApJ, 705, 272
Shimojo, M., Hudson, H. S., White, S. M., Bastian, T. S., & Iwai, K. 2017, ApJ, 841, L5
Shimojo, M., Kawate, T., Okamoto, T. J., et al. 2020, ApJ, 888, L28
Solanki, S. K., & Steiner, O. 1990, A&A, 234, 519
van Noort, M. J., & Rouppe van der Voort, L. H. M. 2006, ApJ, 648, L67
Vernazza, J. E., Avrett, E. H., & Loeser, R. 1981, ApJS, 45, 635
Wedemeyer, S., Freytag, B., Steffen, M., Ludwig, H. G., & Holweger, H. 2004, A&A, 414, 1121
Wedemeyer, S., Bastian, T., Brajša, R., et al. 2016, Space Sci. Rev., 200, 1
Wedemeyer-Böhm, S., Ludwig, H. G., Steffen, M., Leenaarts, J., & Freytag, B. 2007, A&A, 471, 977
Wedemeyer-Böhm, S., Lagg, A., & Nordlund, Å. 2009, Space Sci. Rev., 144, 317
Wedemeyer, S., Szydlarski, M., Jafarzadeh, S., et al. 2020, A&A, 635, A71
Wöger, F., Wedemeyer-Böhm, S., Schmidt, W., & von der Lühe, O. 2006, A&A, 459, L9

Appendix A: Details of synthetic observations

A.1. Specifics of the wavelengths and resolutions

The receiver bands of ALMA are set up for solar observations as four sub-bands (SB), grouped into two pairs of adjacent sub-bands (i.e., for band 3, SB3.1 with SB3.2 and SB3.3 with SB3.4) at equidistant frequency separation from the central (local oscillator) frequency. In Table A.1 we list the specific wavelengths and frequencies for the radiative transfer calculations. Each receiver sub-band has three frequencies, which means ten unique frequencies per receiver band, which are averaged together in the current analysis (note ten and not twelve frequencies because each pair of adjacent sub-bands shares one frequency point).

The angular resolution is dependent on the frequency and the baselines of the interferometric array configuration. The FWHMs of the minor and major axis of the clean beams for each combination of receiver band and array configurations C1–C7 are provided in Table A.2, along with the maximum baseline and the 80 th percentile of the baselines (see Remijan et al. (2020)).

A.2. Millimeter maps at the ALMA receiver bands

Observables at the wavelengths of each spectral ALMA band are presented at the original resolution of the model and at the degraded resolutions corresponding to the the resolution of the most compact interferometric array configuration C1 to increasingly more extended configurations up to C7 (cf. Table. A.2) for each receiver band in Figs A.1 – A.2. The mm maps are given for a single snapshot ($t = 1650$ s), and the color scales are individually given for each band by the span from the minimum brightness temperature to 0.9 times the maximum brightness temperature of the FOV at the original resolution.

A.3. Degradation of T_b excess signatures with limited spatial resolution

In this section, we discuss the density distribution plots of the magnitude of Tb excess signatures at original resolution of the model versus degraded resolutions corresponding to the resulting resolutions of ALMA observations at different spectral bands and with different interferometric array configurations (Figs. A.3–A.6). The three targets with different characteristic magnetic field topologies (QS, FP, and FS) are considered (Fig. 2). Given a spectral band, by direct comparison of the distribution plots at different resolutions in Fig. A.3, it becomes clear that a certain spatial resolution is required to resolve brightening events. At low resolution, the distributions are severely squeezed toward the left and show only small magnitudes that are far from the one-to-one ratio. These plots naturally contribute with slightly more information than the estimates provided by the linear fits in the main text, and we gain a more refined view of the ability to resolve the small-scale brightening events and the uncertainties attached to the resulting values with a specific

Table A.1. Specific wavelengths and frequencies considered in the calculations of the radiative transfer for each of the sub-bands within each ALMA receiver band. In the notation, the sub-bands are preceded by the receiver band. [†]The receiver band is not yet commissioned for solar observations and the frequencies are symmetrically distributed around the "standard continuum" central frequencies (see, i.e., Table 6.1 in the ALMA technical handbook Remijan et al. 2020), similar to those of the commissioned bands.

Sub-band	Wavelength [mm]			Frequency [GHz]		
	min	mid	max	min	mid	max
SB3.1	3.1893	3.2236	3.2586	92.0	93.0	94.0
SB3.2	3.1228	3.1557	3.1893	94.0	95.0	96.0
SB3.3	2.8282	2.8552	2.8826	104.0	105.0	106.0
SB3.4	2.7759	2.8018	2.8282	106.0	107.0	108.0
SB4.1[†]	2.1568	2.1724	2.1883	137.0	138.0	139.0
SB4.2[†]	2.1262	2.1414	2.1568	139.0	140.0	141.0
SB4.3[†]	1.9854	1.9986	2.0120	149.0	150.0	151.0
SB4.4[†]	1.9594	1.9723	1.9854	151.0	152.0	153.0
SB5.1	1.5614	1.5696	1.5779	190.0	191.0	192.0
SB5.2	1.5453	1.5533	1.5614	192.0	193.0	194.0
SB5.3	1.4696	1.4768	1.4841	202.0	203.0	204.0
SB5.4	1.4553	1.4624	1.4696	204.0	205.0	206.0
SB6.1	1.2978	1.3034	1.3091	229.0	230.0	231.0
SB6.2	1.2867	1.2922	1.2978	231.0	232.0	233.0
SB6.3	1.2137	1.2187	1.2236	245.0	246.0	247.0
SB6.4	1.2040	1.2088	1.2137	247.0	248.0	249.0
SB7.1	0.8802	0.8828	0.8854	338.6	339.6	340.6
SB7.2	0.8751	0.8776	0.8802	340.6	341.6	342.6
SB7.3	0.8502	0.8527	0.8551	350.6	351.6	352.6
SB7.4	0.8454	0.8478	0.8502	352.6	353.6	354.6
SB8.1[†]	0.7514	0.7532	0.7551	397.0	398.0	399.0
SB8.2[†]	0.7476	0.7495	0.7514	399.0	400.0	401.0
SB8.3[†]	0.7294	0.7312	0.7330	409.0	410.0	411.0
SB8.4[†]	0.7259	0.7277	0.7294	411.0	412.0	413.0
SB9.1[†]	0.4481	0.4488	0.4495	667.0	668.0	669.0
SB9.2[†]	0.4468	0.4475	0.4481	669.0	670.0	671.0
SB9.3[†]	0.4455	0.4461	0.4468	671.0	672.0	673.0
SB9.4[†]	0.4441	0.4448	0.4455	673.0	674.0	675.0
SB10.1[†]	0.3466	0.3470	0.3474	863.0	864.0	865.0
SB10.2[†]	0.3458	0.3462	0.3466	865.0	866.0	867.0
SB10.3[†]	0.3450	0.3454	0.3458	867.0	868.0	869.0
SB10.4[†]	0.3442	0.3446	0.3450	869.0	870.0	871.0

spectral band, target area, and spatial resolution in mind. Specifically, valuable information here is the span in parameter space of the remaining fraction of events, outside the $\pm 1\sigma$ from the median values, and to which degree the signatures at degraded spatial resolution are represented by apparent brightening events. This means that the cases in which the locations of the brightest events in the degraded data do not show bright events at the original resolution (shown in the lower right corner, below the one-to-one ratio in the graphs).

Table A.2. Clean-beam parameters used in the analysis of the full spectral bands in the realistic good-case scenario with an only slightly elliptical beam. The position angle given in the fifth column is the resulting output from the simulated observations, but all the setups were given the same value of the position angle, $\phi = 80$ deg to enable one-to-one comparisons. The array configurations we used are those for cycle 5 included in the simobserve tool. The ACA array was included. The spectral bands that are not yet commissioned for solar observations (marked with a dagger) are assigned frequencies (cf. Table A.1) according to the standard continuum values (see ALMA cycle 8 technical handbook, Remijan et al. 2020). The array configurations that are not yet commissioned for solar observations with the specific spectral band are marked with an asterisk. The longest baseline of the respective configuration is given in Col. 5 and the 80th percentile baseline in Col. 6 (Remijan et al. 2020).

| Reciever band	Array configuration	Clean beam		Maximum baseline [km]	80th percentile of baselines [km]
		Major axis [arcsec]	Minor axis [arcsec]		
Band 3	C1	3.8809	3.3305	0.1607	0.1071
	C2	2.9258	2.5128	0.3137	0.1438
	C3	1.9682	1.6511	0.5002	0.2354
	C4	1.2329	1.1191	0.7835	0.3692
	C5*	0.7527	0.6916	1.3979	0.6238
	C6*	0.4683	0.3605	2.5169	1.1725
	C7*	0.2862	0.2429	3.6378	1.6731
Band 4†	C1*	2.4849	2.1466	0.1607	0.1071
	C2*	1.8832	1.6250	0.3137	0.1438
	C3*	1.2527	1.0457	0.5002	0.2354
	C4*	0.8256	0.7380	0.7835	0.3692
	C5*	0.5089	0.4691	1.3979	0.6238
	C6*	0.3171	0.2508	2.5169	1.1725
	C7*	0.1954	0.1673	3.6378	1.6731
Band 5	C1	1.8890	1.6405	0.1607	0.1071
	C2	1.4304	1.2370	0.3137	0.1438
	C3	0.9751	0.8211	0.5002	0.2354
	C4*	0.6181	0.5551	0.7835	0.3692
	C5*	0.3762	0.3468	1.3979	0.6238
	C6*	0.2348	0.1842	2.5169	1.1725
	C7*	0.1440	0.1223	3.6378	1.6731
Band 6	C1	1.6215	1.3912	0.1607	0.1071
	C2	1.2330	1.0571	0.3137	0.1438
	C3	0.8247	0.6926	0.5002	0.2354
	C4*	0.5140	0.4651	0.7835	0.3692
	C5*	0.3129	0.2873	1.3979	0.6238
	C6*	0.1983	0.1537	2.5169	1.1725
	C7*	0.1186	0.1024	3.6378	1.6731
Band 7	C1	1.1427	0.9936	0.1607	0.1071
	C2	0.8889	0.7535	0.3137	0.1438
	C3*	0.5881	0.4968	0.5002	0.2354
	C4*	0.3598	0.3250	0.7835	0.3692
	C5*	0.2179	0.2008	1.3979	0.6238
	C6*	0.1371	0.1057	2.5169	1.1725
	C7*	0.0823	0.0713	3.6378	1.6731
Band 8†	C1*	0.9978	0.8685	0.1607	0.1071
	C2*	0.7709	0.6477	0.3137	0.1438
	C3*	0.5030	0.4256	0.5002	0.2354
	C4*	0.3094	0.2811	1.3979	0.6238
	C5*	0.1874	0.1716	0.7835	0.3692
	C6*	0.1165	0.0890	2.5169	1.1725
Band 9†	C1*	0.6178	0.5383	0.7835	0.3692
	C2*	0.4761	0.4002	1.3979	0.6238
	C3*	0.3091	0.2617	0.5002	0.2354
	C4*	0.1874	0.1705	0.3137	0.1438
	C5*	0.1137	0.1034	0.1607	0.1071
Band 10†	C1*	0.4779	0.4168	0.7835	0.3692
	C2*	0.3730	0.3112	1.3979	0.6238
	C3*	0.2397	0.2035	0.5002	0.2354
	C4*	0.1463	0.1312	0.3137	0.1438
	C5*	0.0887	0.0799	0.1607	0.1071
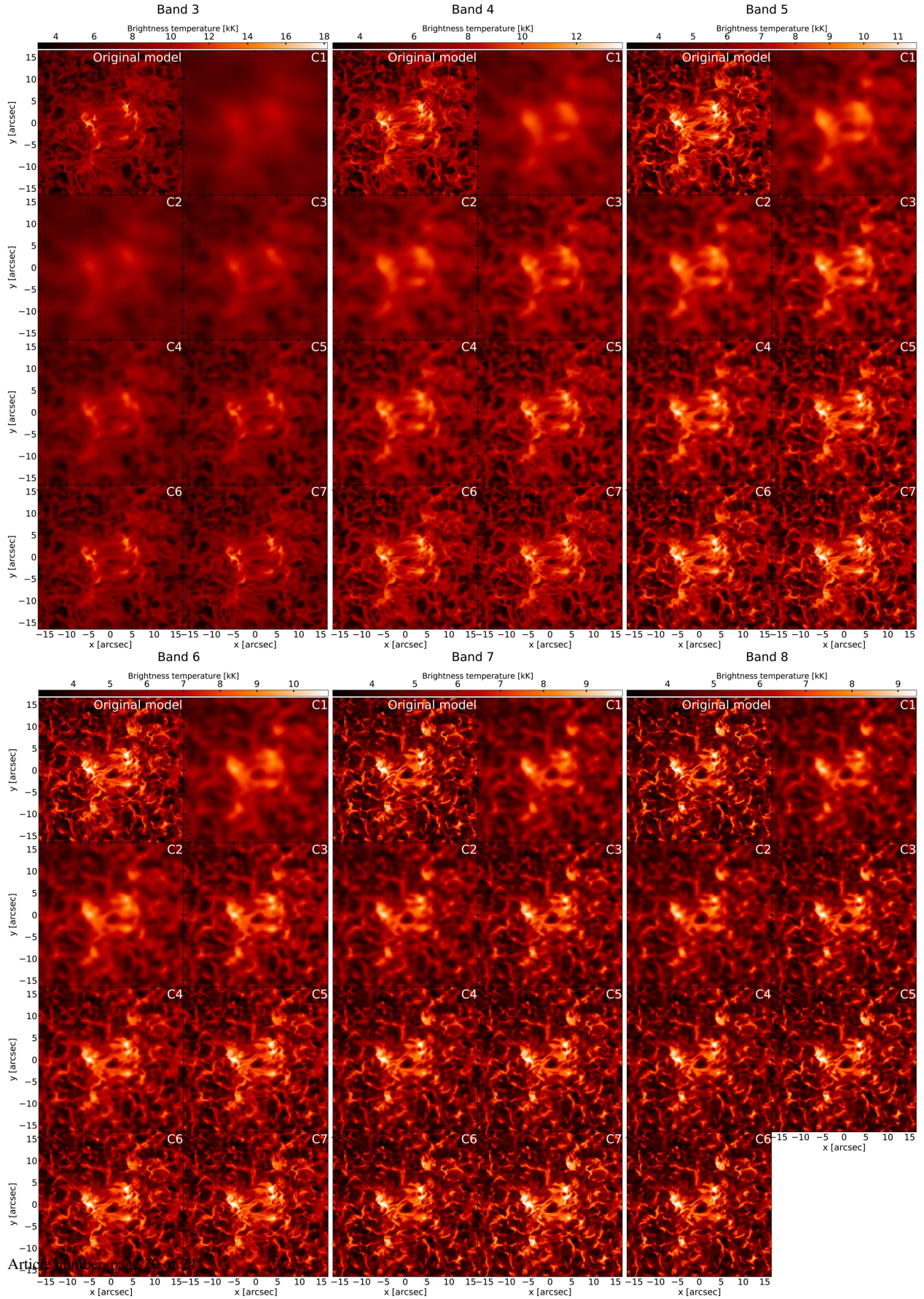
Fig. A.1. FOV of observables at spectral bands 3–8 and at spatial resolutions corresponding to array configurations C1-C7 (up to C6 for band 8; Table A.2). The color code of each band spans the minimum and 0.9 times the maximum values of the respective FOV at the original resolution.
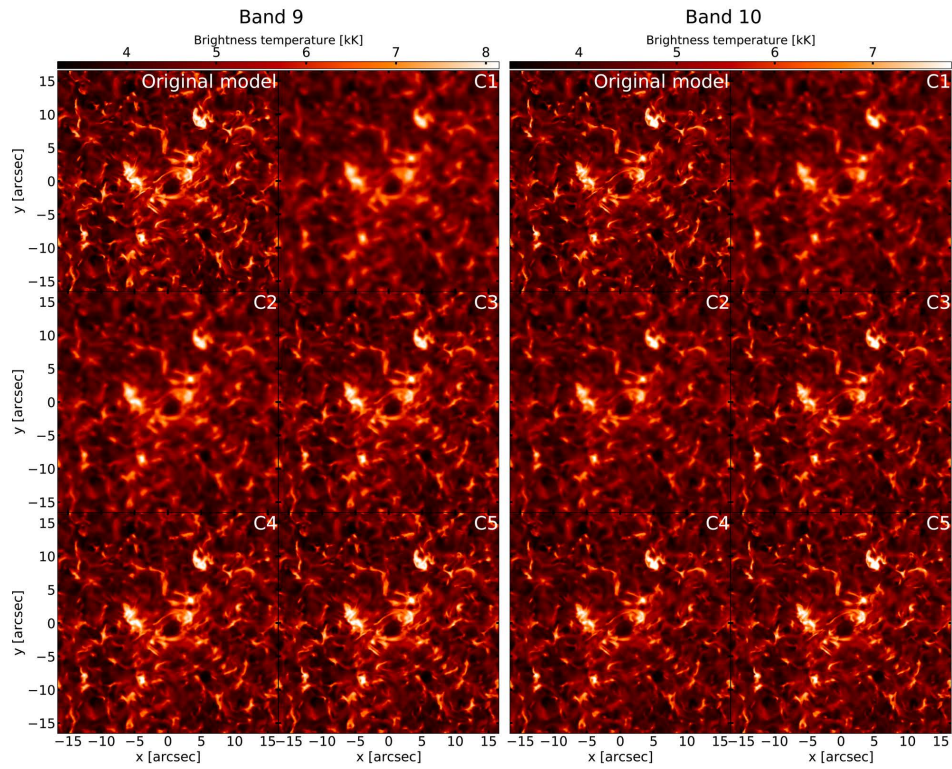
Fig. A.2. FOV of observables at spectral bands 9–10 and at spatial resolutions corresponding to array configurations C1-C5 (Table A.2). The color code of each band spans the minimum and 0.9 times the maximum values of the respective FOV at the original resolution.

Fig. A.3. Bands 3 and 4. Density plots of brightening events at the original resolution vs. degraded resolution. Columns show spectral band and target region from left to right: band 3 QS, FS, FP, and band 4 QS, FS and FP. Rows from top to bottom show the resolutions of array configurations C1 – C7.
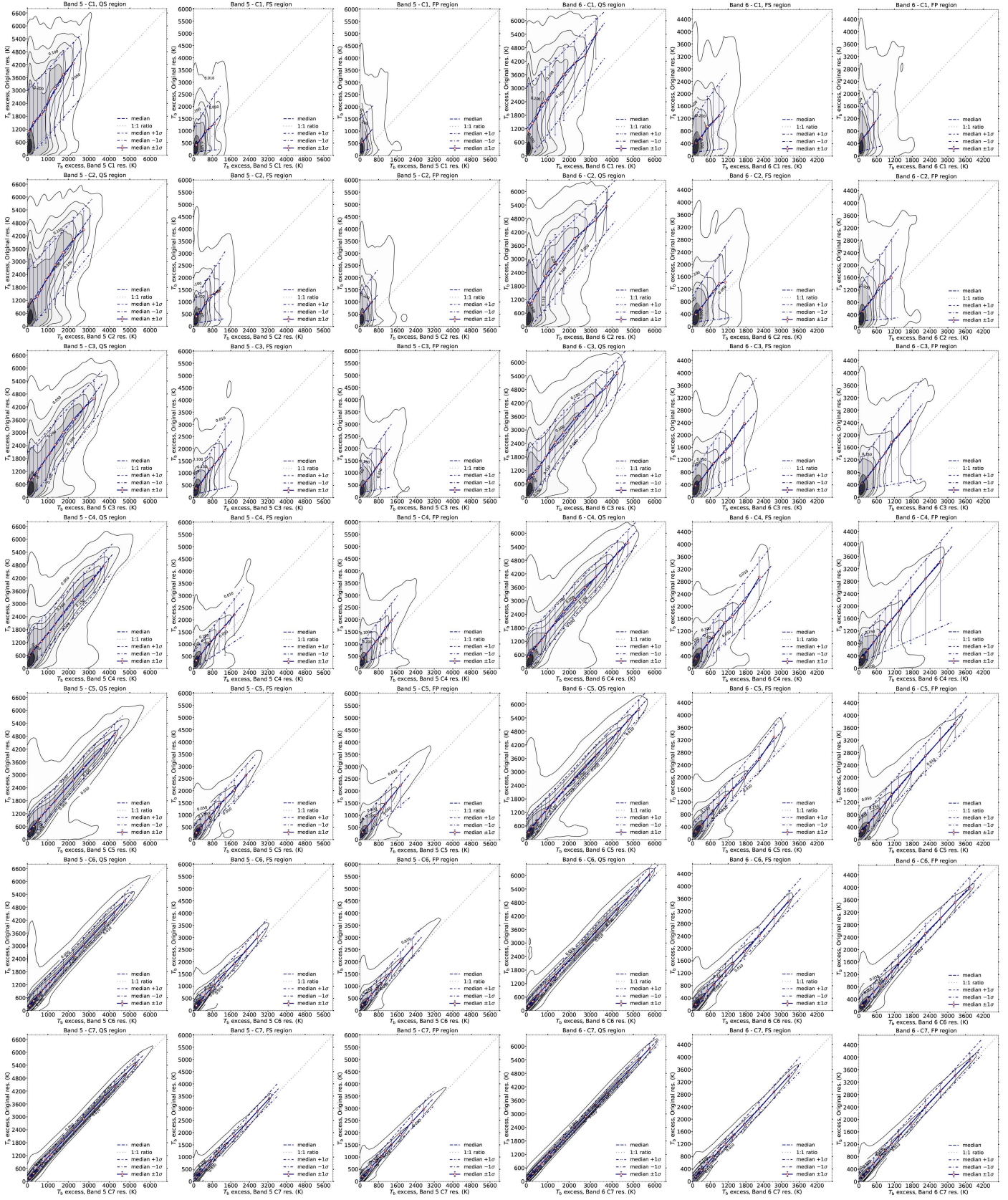
Fig. A.4. Bands 5 and 6. Density plots of brightening events at the original resolution vs. degraded resolution. Columns show spectral band and target region from left to right: band 5 QS, FS, FP, and band 6 QS, FS and FP. Rows from top to bottom show the resolutions of array configurations C1 – C7.
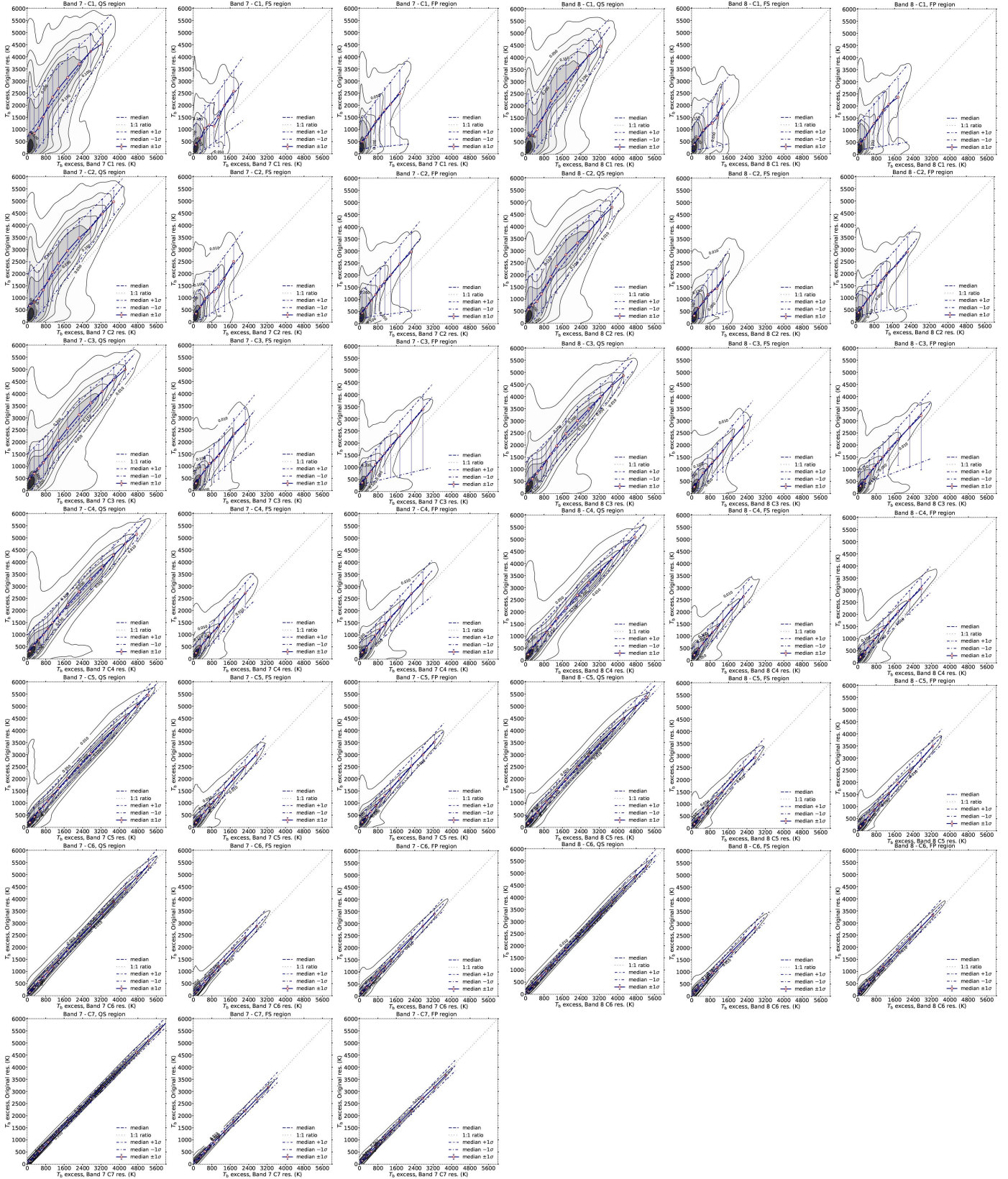
Fig. A.5. Bands 7 and 8. Density plots of brightening events at the original resolution vs. degraded resolution. Columns show spectral band and target region from left to right: band 7 QS, FS, FP, and band 8 QS, FS and FP. Rows from top to bottom show the resolutions of array configurations C1 – C7 (limited to C6 for band 8).
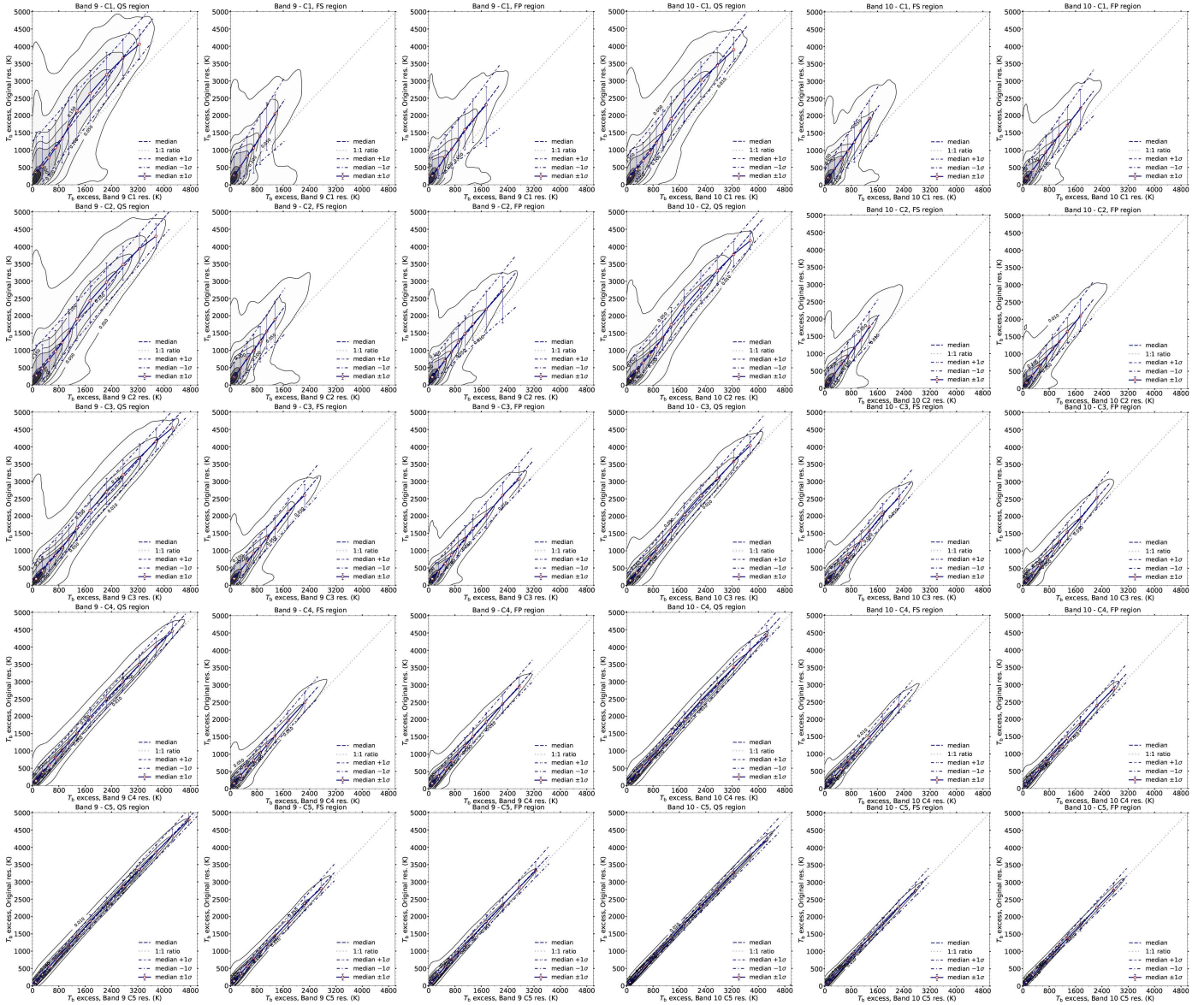
Fig. A.6. Bands 9 and 10. Density plots of brightening events at the original resolution vs. degraded resolution. Columns show spectral band and target region from left to right: band 9 QS, FS, FP, and band 10 QS, FS and FP. Rows from top to bottom show the resolutions of array configurations C1 – C5.